



Numerical assessments of high-order accurate shock capturing schemes: Kelvin–Helmholtz type vortical structures in high-resolutions



Omer San ^{a,*}, Kursat Kara ^b

^aInterdisciplinary Center for Applied Mathematics, Virginia Tech, Blacksburg, VA, USA

^bDepartment of Aerospace Engineering, Khalifa University, Abu Dhabi, United Arab Emirates

ARTICLE INFO

Article history:

Received 6 August 2013

Received in revised form 10 October 2013

Accepted 6 November 2013

Available online 16 November 2013

ABSTRACT

This paper investigates performance of extensions of the state-of-the-art high-resolution shock capturing schemes by solving hyperbolic conservation laws in gas dynamics. Such numerical schemes used for the integration of compressible flow simulations should provide accurate solutions for the long time integrations these flows require. To this end, several joint solvers are developed within the framework of the reconstruction and flux-splitting approaches using the underlying MUSCL and WENO frameworks. The numerical assessments include testing and evaluation of various interpolation procedures, flux-limiters, Riemann solvers, flux-splitting schemes as well as their formal order of accuracy. A three-stage optimal TVD Runge–Kutta time stepping is employed for temporal integration. The modular development of these joint solvers provides an ease in characterizing the solution procedures. The performances of these high-resolution solvers are compared for several carefully selected two-dimensional Riemann problems including shock and rarefaction waves as well as joint discontinuities. Based on solutions obtained by all forms of five-point stencil schemes, we demonstrate that the reconstruction based WENO scheme with Roe solver is more accurate than all the versions of the flux-splitting WENO solvers tested in this study. We also show that results are highly dependent on the choice of the flux limiter. Performing benchmark quality high-resolution computations, it is shown that the Euler equations discretized by the fifth-order WENO scheme produce solutions which convect vorticity and create small-scale vortical flow structures which are usually associated with the high Reynolds number viscous flows. Surprisingly, it is found that these Kelvin–Helmholtz instability like vortical structures are not captured in any form of the third-order five-point stencil schemes.

© 2013 Elsevier Ltd. All rights reserved.

1. Introduction

Computational studies of compressible flow problems are important in basic scientific research, and for a multitude of engineering applications. In the decades since the first compressible flow computations were performed, many successful shock-capturing algorithms have been proposed for computing these flows [1–6]. The holy grail is to obtain a sharp discontinuity effectively, extending over as few grid points as possible. Terms like essentially non-oscillatory, monotone upwind, or total variation diminishing (TVD) are applied to various methods for capturing shocks via some sort of numerical dissipation which is a consequence of physics that produce an upwind bias in these algorithms. This numerical dissipation can provide stability and robustness, without significantly deteriorating accuracy.

The design of an efficient and reliable shock capturing algorithm is often a challenge. The implementation of low-dissipation

centered schemes usually result in spurious Gibbs oscillations in convection-dominated or discontinuous flows due to spectral truncation in the wavenumber space. In order to prevent the appearance of Gibbs oscillations in simulations of shock dominated flows, the usual approach is to develop upwind-biased schemes [7]. A numerical scheme must possess sufficient dissipation to capture strong shocks without developing overshoots and oscillations in the vicinity of the discontinuity. Although several high-order methods for computing shocks, such as monotone upwind-central schemes for conservation laws (MUSCL) schemes making use of flux or slope limiters and weighted essentially non-oscillatory (WENO) schemes in which an adaptative stencil that adjusts to the smoothness of the solutions is applied, have been developed, none of them has yet set a standard state-of-the art. Many of these methods are based on the detection of the shocks and on the reconstruction of lower-order, oscillation-free, solutions on corresponding cells. The reader is referred for instance to the two reviews made by Shu [8] and Pirozzoli [9] for more details.

Such shock capturing methods can be classified as reconstruction or flux-splitting based approaches. In the first approach,

* Corresponding author.

E-mail address: omersan@vt.edu (O. San).

reconstructed left and right states are determined at cell edges using interpolation procedures such as MUSCL or WENO reconstructions, then a Riemann solver is usually adopted to calculate fluxes through these cell boundaries. Approximate Riemann solvers such as those developed by Roe [10] or Harten et al. (HLL) [11] are widely used because of their numerical accuracy and robustness. The latter approach requires a flux-splitting procedure, depending on the direction in which the information is propagating, to obtain positive and negative fluxes at the cell centers, and then an interpolation procedure can be used to compute both fluxes at the cell boundaries (e.g., see [12] for WENO schemes).

As illustrated by the broad range of algorithms for the Euler equations (as well as other systems of hyperbolic conservation laws) in the literature over the past three decades, a number of various strategies have been used to approximately construct the conservative flux values, which allow accurate and robust representation of shocks without introducing non-physical oscillations or excessive diffusion into the solution. Analyzing the performance of these algorithms is a challenging task because such methods are typically verified using different benchmark problems. However, there are several intercomparison studies targeted for different purposes [13–18]. Liska and Wendroff [14] presented a comprehensive study by comparing eight shock capturing methods (including the third-order accurate piecewise parabolic method, the fifth-order accurate WENO method and several second-order accurate schemes such as the positive scheme of Lax and Liu [19]) for solving various one-dimensional and two-dimensional test problems to draw some conclusions about the applicability of these methods. They showed that some methods appear to work better than others on a specific problem, but no one scheme has shown itself to be superior at all. Based on a set of one-dimensional test problems, Greenough and Rider [15] concluded that a second-order Godunov type scheme provides more accuracy per computational cost than a fifth-order WENO scheme. A comprehensive range of high-resolution methods (WENO, hybrid WENO/central difference, artificial diffusivity, adaptive characteristic-based filter, and shock fitting) have also been presented by Johnsen et al. [18] for a suite of test cases relevant to problems with shocks and turbulence. Their results indicated that the WENO methods provide sharp shock profiles, but overwhelm the physical dissipation while the shock fitting approach, where shock waves are explicitly introduced in the solution using appropriate shock relations, yielded good results. However, these studies are invaluable for better understanding of various numerical methods for hyperbolic conservation laws, it is difficult to determine which method is the most appropriate. Different than the published comparative studies described above, our comparisons here focus on the effects of various sub-strategies to approximate the conservative fluxes by considering several interpolation procedures, flux-limiters, Riemann solvers and flux-splitting schemes.

In the present study, a comparative modular framework is designed for developing high-order accurate shock capturing algorithms. The variants of MUSCL and WENO methods are considered and compared for their effectiveness and their ability to accurately compute flows with strong shocks on a variety of two-dimensional test cases. The goal of this paper is threefold: First, it investigates the effect of several reconstruction procedures in combination with various Riemann solvers at the cell interfaces. Several variants of flux-limiter based MUSCL reconstruction procedures are compared with the WENO reconstruction procedure which is based on the idea of nonlinear weights with the smoothness indicators. The effects of the use of different flux-limiters on the solution accuracy are also demonstrated. Second, it compares these reconstruction based schemes with various forms of flux-splitting WENO schemes without using a Riemann solver at the cell interfaces. Third, it investigates the effects of flux-splitting meth-

ods on the accuracy of the third- and fifth-order WENO schemes for solving two-dimensional Euler equations on different resolutions. The joint solvers with local Lax–Friedrichs [20], Steger and Warming [21] and Van Leer [22] flux-splitting procedures are applied to several Riemann problems including shock and rarefaction waves as well as contact discontinuities. Performing benchmark quality high-resolution computations, it is serendipitously discovered that the Euler equations discretized by the fifth-order WENO scheme with all the forms of splitting methods produce solutions that convect vorticity and create small-scale vortical flow structures which are usually associated with the high Reynolds number viscous flows. These Kelvin–Helmholtz instability like vortical structures are not captured or generated in any forms of the third-order WENO or MUSCL schemes at any resolutions considered in our numerical experiments. Since the vorticity is generated as a result of a discontinuity in the flow field, according to the Crocco–Vazonski equations (see Thompson [23] for a derivation), these solutions can be considered valid and accurate solutions to the Euler equations.

The paper is organized as follows: Euler equations, the governing equations for inviscid compressible flows, are briefly introduced in Section 2. The numerical methods are presented in Section 3 by using a modular approach with joint reconstruction and flux-splitting algorithms. The results for these joint solvers are presented in Section 4. Finally, the conclusions and some comments on the performance of these schemes are summarized in Section 5.

2. Euler equations in gas dynamics

The two-dimensional Euler equations can be represented in the conservation form as

$$\frac{\partial q}{\partial t} + \frac{\partial F}{\partial x} + \frac{\partial G}{\partial y} = 0 \quad (1)$$

where

$$q = \begin{pmatrix} \rho \\ \rho u \\ \rho v \\ \rho e \end{pmatrix}, \quad F = \begin{pmatrix} \rho u \\ \rho u^2 + p \\ \rho uv \\ \rho uH \end{pmatrix}, \quad G = \begin{pmatrix} \rho v \\ \rho uv \\ \rho v^2 + p \\ \rho vH \end{pmatrix}$$

in which

$$H = e + p/\rho, \quad p = \rho(\gamma - 1)\left(e - \frac{1}{2}(u^2 + v^2)\right). \quad (2)$$

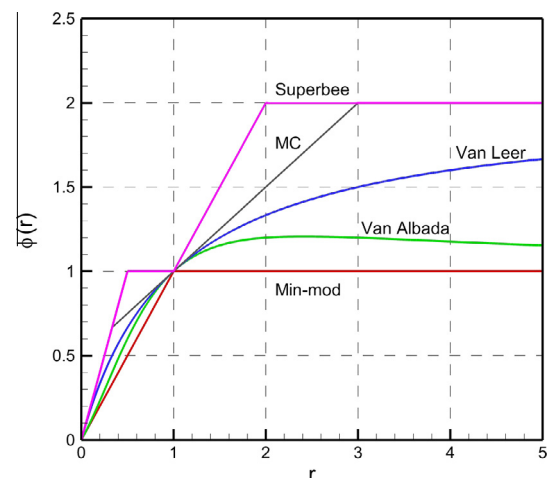


Fig. 1. Flux limiters considered in this study.

Here, ρ, p, u , and v are respectively the density, pressure, horizontal and vertical components of the velocity; e and H denote the internal energy and static enthalpy; γ is the ratio of specific heats. The eigen-system of the equations will be used extensively in developing numerical methods applied to the hyperbolic conservation laws. In two-dimensional Euler equations, the convective flux Jacobian matrices are

$$A = \frac{\partial F}{\partial q} = \begin{pmatrix} 0 & 1 & 0 & 0 \\ \phi^2 - u^2 & (3 - \gamma)u & -(\gamma - 1)v & \gamma - 1 \\ -uv & v & u & 0 \\ (\phi^2 - H)u & H - (\gamma - 1)u^2 & -(\gamma - 1)uv & \gamma u \end{pmatrix}$$

$$B = \frac{\partial G}{\partial q} = \begin{pmatrix} 0 & 0 & 1 & 0 \\ -uv & v & u & 0 \\ \phi^2 - v^2 & -(\gamma - 1)u & (3 - \gamma)v & \gamma - 1 \\ (\phi^2 - H)v & -(\gamma - 1)uv & H - (\gamma - 1)v^2 & \gamma v \end{pmatrix}$$

where $\phi^2 = \frac{1}{2}(\gamma - 1)(u^2 + v^2)$. Because this system is hyperbolic, there exists a similarity transform, such that,

$$LAR = A \Rightarrow A = RAL$$

$$SBT = \Psi \Rightarrow B = T\Psi S$$

where A and Ψ are respectively the diagonal matrices of the real eigenvalues of A and B ; R and T are the matrices, the columns of which are the right eigenvectors of A and B ; $L = R^{-1}$ and $S = T^{-1}$ are the matrices, the rows of which are the left eigenvectors of A and B . These matrices can be written as [24]

$$R = \begin{pmatrix} 1 & 0 & \beta & \beta \\ u & 0 & \beta(u+a) & \beta(u-a) \\ v & -1 & \beta v & \beta v \\ \frac{\phi^2}{(\gamma-1)} & -v & \beta(H+ua) & \beta(H-ua) \end{pmatrix}$$

$$L = \begin{pmatrix} 1 - \frac{\phi^2}{a^2} & (\gamma - 1)\frac{u}{a^2} & (\gamma - 1)\frac{v}{a^2} & -\frac{(\gamma-1)}{a^2} \\ v & 0 & -1 & 0 \\ \phi^2 - ua & a - (\gamma - 1)u & -(\gamma - 1)v & \gamma - 1 \\ \phi^2 + ua & -a - (\gamma - 1)u & -(\gamma - 1)v & \gamma - 1 \end{pmatrix}$$

$$T = \begin{pmatrix} 1 & 0 & \beta & \beta \\ u & 1 & \beta u & \beta u \\ v & 0 & \beta(v+a) & \beta(v-a) \\ \frac{\phi^2}{(\gamma-1)} & u & \beta(H+va) & \beta(H-v a) \end{pmatrix}$$

$$S = \begin{pmatrix} 1 - \frac{\phi^2}{a^2} & (\gamma - 1)\frac{u}{a^2} & (\gamma - 1)\frac{v}{a^2} & -\frac{(\gamma-1)}{a^2} \\ -u & 1 & 0 & 0 \\ \phi^2 - va & -(\gamma - 1)u & a - (\gamma - 1)v & \gamma - 1 \\ \phi^2 + va & -(\gamma - 1)u & -a - (\gamma - 1)v & \gamma - 1 \end{pmatrix}$$

$$A = \begin{pmatrix} u & 0 & 0 & 0 \\ 0 & u & 0 & 0 \\ 0 & 0 & u+a & 0 \\ 0 & 0 & 0 & u-a \end{pmatrix}, \quad \Psi = \begin{pmatrix} v & 0 & 0 & 0 \\ 0 & v & 0 & 0 \\ 0 & 0 & v+a & 0 \\ 0 & 0 & 0 & v-a \end{pmatrix}$$

where a is the speed of the sound and defined as $a^2 = \gamma p/\rho$, and $\beta = 1/(2a^2)$. Although the eigenvalue matrices A and Ψ are uniquely defined in the system, it should be noticed that there are infinitely many choices of eigenvectors. It should be noted that the chosen set of eigenvectors can slightly affect the results for certain

algorithms [25], the results in this paper, however, are invariant of the selection of the eigenvectors.

3. Numerical methods

Many computational algorithms have been developed for compressible flows governed by hyperbolic conservation laws. In this section, we briefly introduce some variants of the state-of-art shock capturing schemes. The semi-discrete form of the Euler equations given in Eq. (1) is

$$\frac{dq_{ij}}{dt} + \frac{1}{\Delta x} (F_{i+1/2,j} - F_{i-1/2,j}) + \frac{1}{\Delta y} (G_{i,j+1/2} - G_{i,j-1/2}) = 0 \quad (3)$$

where q_{ij} is the cell averaged vector of dependant variables; $F_{i\pm 1/2,j}$ are the fluxes at the left and right cell boundaries, and $G_{i,j\pm 1/2}$ are the fluxes at the bottom and top cell boundaries. To implement the Runge–Kutta schemes for the time integration, we cast the model equations in the following form

$$\frac{dq}{dt} = \mathcal{E}(q) \quad (4)$$

where $\mathcal{E}(q)$ is the discrete operator representing the convective flux terms. We assume that the numerical approximation for time level n is known, and we seek the numerical approximation for time level $n + 1$, after the time step Δt . The optimal third-order accurate total variation diminishing Runge–Kutta (TVDRK3) scheme is then given as [26,27]

$$\begin{aligned} q^{(1)} &= u^n + \Delta t \mathcal{E}(q^n) \\ q^{(2)} &= \frac{3}{4}q^n + \frac{1}{4}q^{(1)} + \frac{1}{4}\Delta t \mathcal{E}(q^{(1)}) \\ q^{n+1} &= \frac{1}{3}q^n + \frac{2}{3}q^{(2)} + \frac{2}{3}\Delta t \mathcal{E}(q^{(2)}) \end{aligned} \quad (5)$$

where the time step should be given by

$$\Delta t = \min \left(\eta \frac{\Delta x}{\max(|A|)}, \eta \frac{\Delta y}{\max(|\Psi|)} \right) \quad (6)$$

in which $\max(|A|)$ and $\max(|\Psi|)$ represents the maximum absolute eigenvalues over the entire spatial domain at known time level. Here, $\eta \leq 1$ for numerical stability. In this study, we use $\eta = 0.5$ for all the computations. The TVDRK3 scheme has been extensively used to compute hyperbolic conservation laws (e.g., see [28–32]). In addition to its TVD property, it has been also shown that the TVDRK3 predicts slightly more accurate results than some other third-order Runge–Kutta schemes for solving incompressible flow problems [33].

3.1. Reconstruction schemes

In this concept, for each cell, reconstructed left and right states are determined and used to calculate fluxes at cell edges. It consists of two basic procedures: (i) the selection of the interpolation procedure to estimate the solution at the interface boundaries from the solution available at the cell centers, (ii) the selection of the Riemann solver to determine the flux from the reconstructed left and right states at the cell boundaries. In the semi-discrete form given by Eq. (3) the fluxes at the interfaces are functions of left (bottom in y -direction) and right (top in y -direction) reconstructed states. In the following, we will omit the spatial index which is not in the direction of the action. We only present the schemes showing the procedures in x -direction, however, the same procedures are applied in y -direction.

3.1.1. MUSCL reconstruction

The simplest reconstruction scheme is defined as

$$q_{i+1/2}^L = q_i, \quad q_{i-1/2}^R = q_i \quad (7)$$

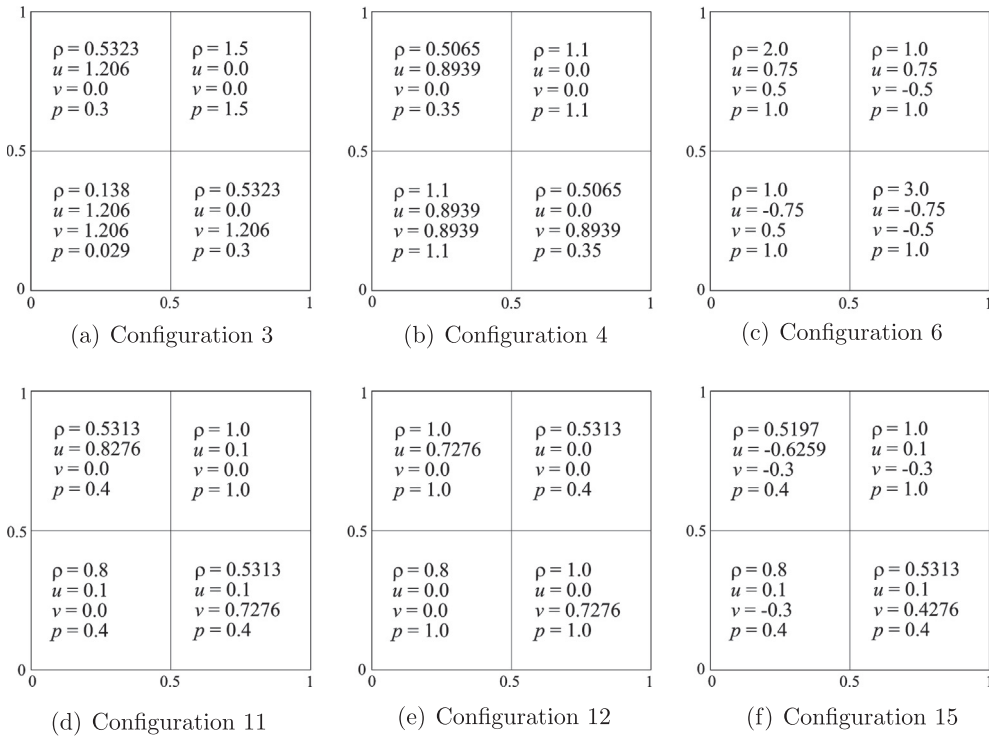


Fig. 2. Initial conditions for six two-dimensional Riemann problems defined by Lax and Liu [19].

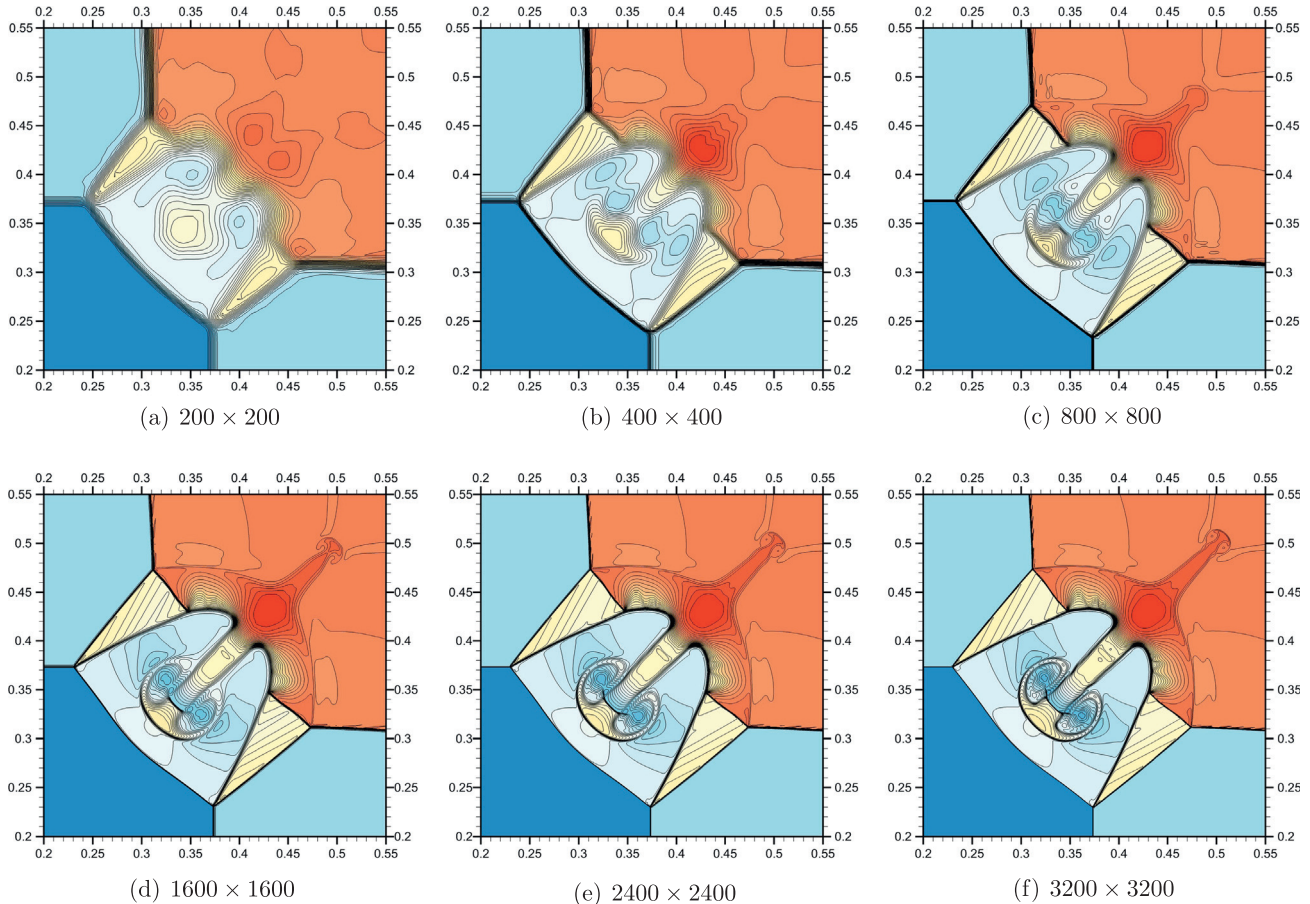


Fig. 3. Configuration 3 of Lax and Liu [19] at time $t = 0.3$. Grid independence study performed by MUSCL-KT scheme with Van Albada flux limiter. The 41 equidistant contour lines are shown between the density levels of 0.2 and 1.7 inclusively.

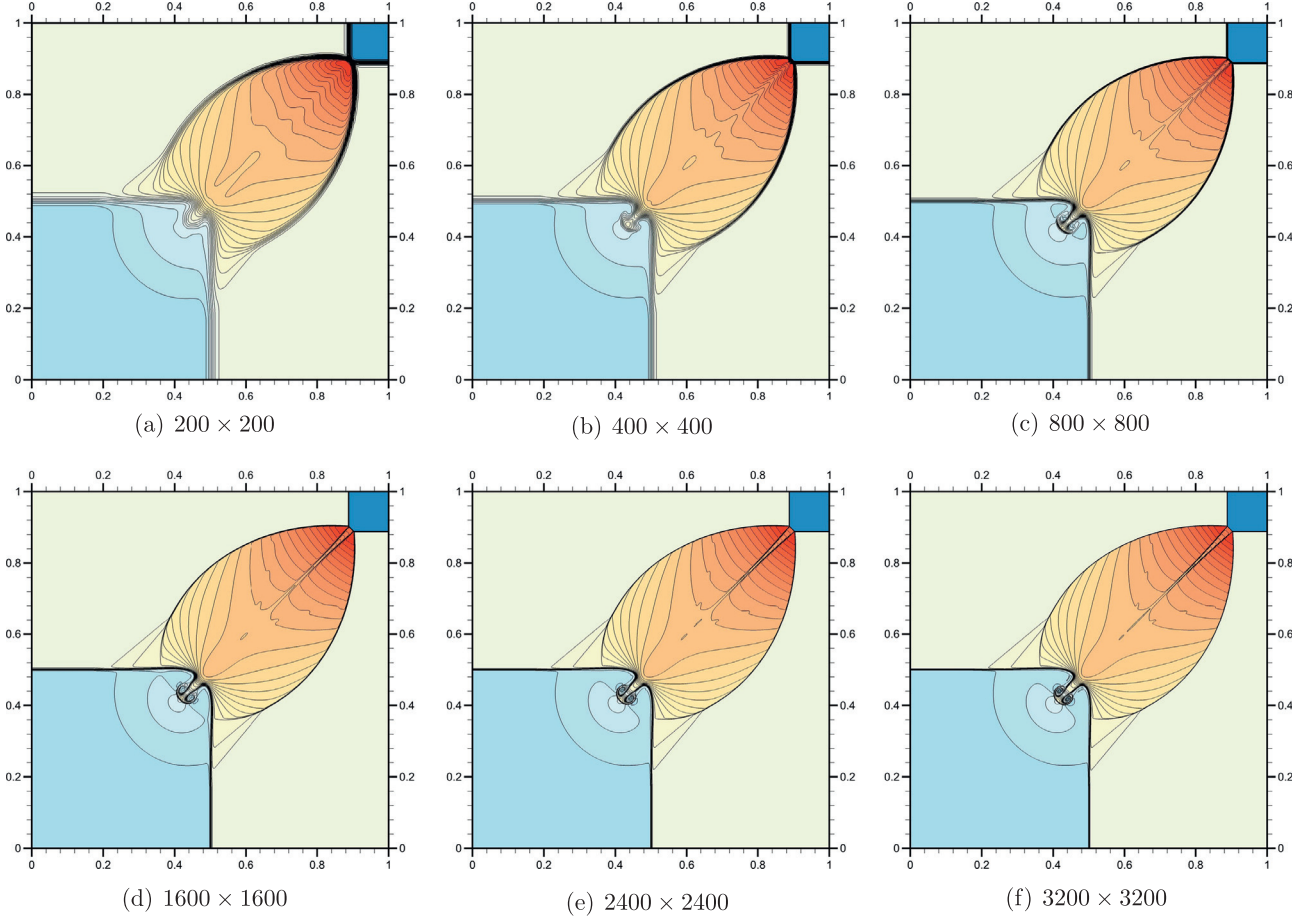


Fig. 4. Configuration 12 of Lax and Liu [19] at time $t = 0.25$. Grid independence study performed by MUSCL-KT scheme with Van Albada flux limiter. The 41 equidistant contour lines are shown between the density levels of 0.55 and 1.65 inclusively.

where left and right states are obtained using the first-order approximations. The resulting scheme preserves monotonicity (i.e., non-oscillatory behavior without producing a new maximum or minimum), but it is too diffusive. An established choice for the high-order interpolation procedure known as Monotone Upwind-central Schemes for Conservation Laws (MUSCL) was originally pioneered by Van Leer in his seminal papers [34–36]. MUSCL denotes a family of interpolation schemes and many variants were proposed using the same acronym [37–39]. Flux limiters allows to limit the slope of the forward and backward gradients in such a way that the interpolated points do not create a new maximum or minimum. Near the discontinuity, limiters cause the discretization to become a first-order upwind approximation, while away from the discontinuity, the flux limitation is removed and the numerical accuracy becomes high-order (i.e., second or third for five point stencil schemes). A one parameter family of MUSCL scheme can be defined for any given cell as

$$q_{i+1/2}^L = q_i + \frac{1}{4} \left[(1 - \kappa) \phi\left(\frac{1}{r}\right) (q_i - q_{i-1}) + (1 + \kappa) \phi(r) (q_{i+1} - q_i) \right] \quad (8)$$

$$q_{i-1/2}^R = q_i - \frac{1}{4} \left[(1 + \kappa) \phi\left(\frac{1}{r}\right) (q_i - q_{i-1}) + (1 - \kappa) \phi(r) (q_{i+1} - q_i) \right] \quad (9)$$

where $\phi(r)$ is the limiter function. The difference ratio r is defined as

$$r = \frac{q_i - q_{i-1}}{q_{i+1} - q_i}. \quad (10)$$

Various limiter functions have been developed in the literature and are currently applied [39] for capturing shocks. Van Leer [34] proposed initially the formula

$$\phi_{vl}(r) = \frac{r + |r|}{1 + r}; \quad \lim_{r \rightarrow \infty} \phi_{vl}(r) = 2. \quad (11)$$

A similar limiter has been applied by Van Albada et al. [40]

$$\phi_{va}(r) = \frac{r^2 + r}{r^2 + 1}; \quad \lim_{r \rightarrow \infty} \phi_{va}(r) = 1. \quad (12)$$

Sweby [2] showed the admissible limiter region for second-order monotonicity domain, which is also called as second-order TVD region. TVD means that the sum of all the step differences between adjacent points must remain the same or decrease as time progress. The lowest boundary of the considered TVD domain, showing the most dissipative behavior, is an often applied as a limiter. It is known as min-mod limiter

$$\phi_{mm}(r) = \max(0, \min(r, 1)); \quad \lim_{r \rightarrow \infty} \phi_{mm}(r) = 1. \quad (13)$$

On the other hand, the upper limit of the domain has been considered by Roe [41] referring superbee limiter

$$\phi_{sb}(r) = \max(0, \min(2r, 1), \min(r, 2)); \quad \lim_{r \rightarrow \infty} \phi_{sb}(r) = 2. \quad (14)$$

In between, Van Leer also proposed the monotonized central (MC) flux limiter [35]

$$\phi_{mc}(r) = \max(0, \min(2r, 0.5(1+r), 2)); \quad \lim_{r \rightarrow \infty} \phi_{mc}(r) = 2. \quad (15)$$

Superbee limiter leads to very sharp non-diffusive behavior and it is possible that some contributions are enhanced instead of reduced, while remaining within the TVD region. The Van Leer, Van Albada and monotonized central limiters have properties between the

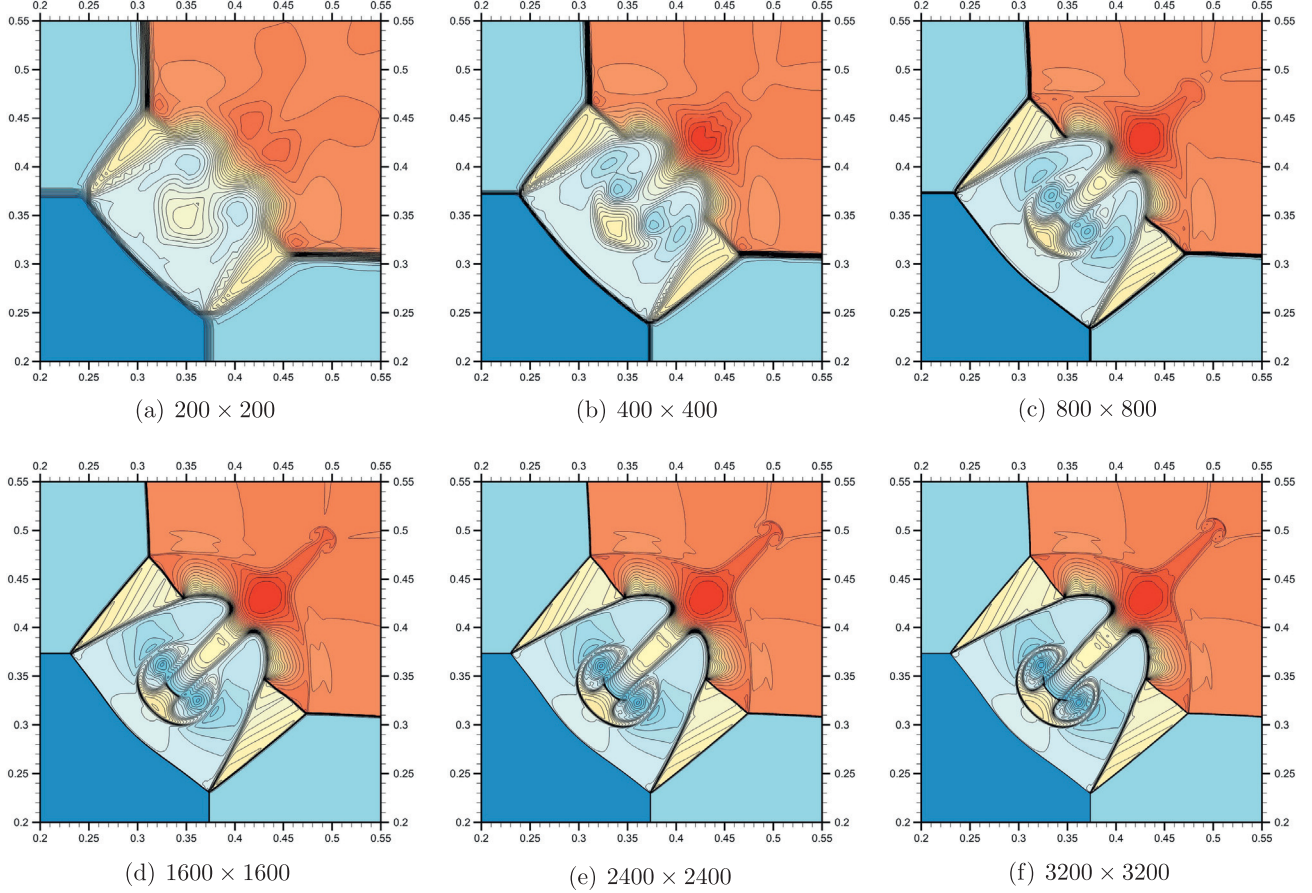


Fig. 5. Configuration 3 of Lax and Liu [19] at time $t = 0.3$. Grid independence study performed by WENO3-S-LFR scheme. The 41 equidistant contour lines are shown between the density levels of 0.2 and 1.7 inclusively.

min-mod and superbee limiters as shown in Fig. 1. These limiters are also called symmetric, exhibit the following symmetry property:

$$\phi\left(\frac{1}{r}\right) = \frac{\phi(r)}{r}. \quad (16)$$

This symmetry condition is a desirable property as it ensures that the limiting actions for forward and backward gradients operate in the same way. In this study, we will investigate effects of these limiters on the solution of two-dimensional Riemann problems.

The valid range for the parameter κ in Eq. (8) and Eq. (9) is between $-1 \leq \kappa \leq 1$. In the absence of the limiter function, a value of less than one results in an upwind biased scheme, while a value of exactly $\kappa = 1$ results in a centered scheme (i.e., Lax-Wendroff scheme). A fully second-order upwind scheme is obtained by setting $\kappa = -1$. Fromm scheme [42] defined by the average of the Lax-Wendroff and the second-order upwind schemes is obtained by setting $\kappa = 0$. Any value of parameter κ results in a second-order reconstruction with an exception of $\kappa = 1/3$, which results in a unique third-order accurate reconstruction. The scheme is referred as Quick scheme [39] when $\kappa = 1/2$.

Another type MUSCL interpolation scheme was used by Nessyahu and Tadmor [43] and Kurganov and Tadmor [44]:

$$q_{i+1/2}^L = q_i + \frac{1}{2}\phi(r)(q_{i+1} - q_i) \quad (17)$$

$$q_{i-1/2}^R = q_i - \frac{1}{2}\phi(r)(q_{i+1} - q_i) \quad (18)$$

which is denotes as MUSCL-KT in this study. This can be considered as a special case of the one-parameter family of MUSCL scheme (i.e., $\kappa = 1$ in Eq. (8), and $\kappa = -1$ in Eq. (9)). It should be noted that Eq.

(17) and Eq. (18) can be recovered from Eq. (8) and Eq. (9) when using a symmetric flux limiter without any dependency in κ .

3.1.2. WENO reconstruction

Weighted essentially non-oscillatory (WENO) reconstruction is another widely used method to construct left and right states at the cell boundaries from the solution available at the cell centers [45]. Similar to the MUSCL schemes presented above, the five-point stencil WENO reconstruction procedures, also known as the third-order WENO reconstruction, can be written in the following form

$$q_{i+1/2}^L = \frac{w_1}{2}(-q_{i-1} + 3q_i) + \frac{w_2}{2}(q_i + q_{i+1}) \quad (19)$$

$$q_{i-1/2}^R = \frac{w_1}{2}(q_{i-1} + q_i) + \frac{w_2}{2}(3q_i - q_{i+1}) \quad (20)$$

where nonlinear weights are defined as

$$w_1 = \frac{\alpha_1}{\alpha_1 + \alpha_2}, \quad w_2 = \frac{\alpha_2}{\alpha_1 + \alpha_2}; \quad \alpha_1 = \frac{d_1}{(\beta_1 + \epsilon)^2}, \quad \alpha_2 = \frac{d_2}{(\beta_2 + \epsilon)^2} \quad (21)$$

in which the smoothness indicators are defined as

$$\beta_1 = (q_i - q_{i-1})^2, \quad \beta_2 = (q_{i+1} - q_i)^2 \quad (22)$$

where the larger this smoothness indicator β_j , the less smooth the function q is in the stencil. Therefore, if there is a discontinuity in the stencil, its weights approaches to zero, and the other stencil becomes effective. Linear weighting coefficients are $d_1 = 1/3$ and $d_2 = 2/3$ in Eq. (19), and $d_1 = 2/3$ and $d_2 = 1/3$ in Eq. (20). It is typical to set $\epsilon = 10^{-6}$ for eliminating zero denominators. In this study,

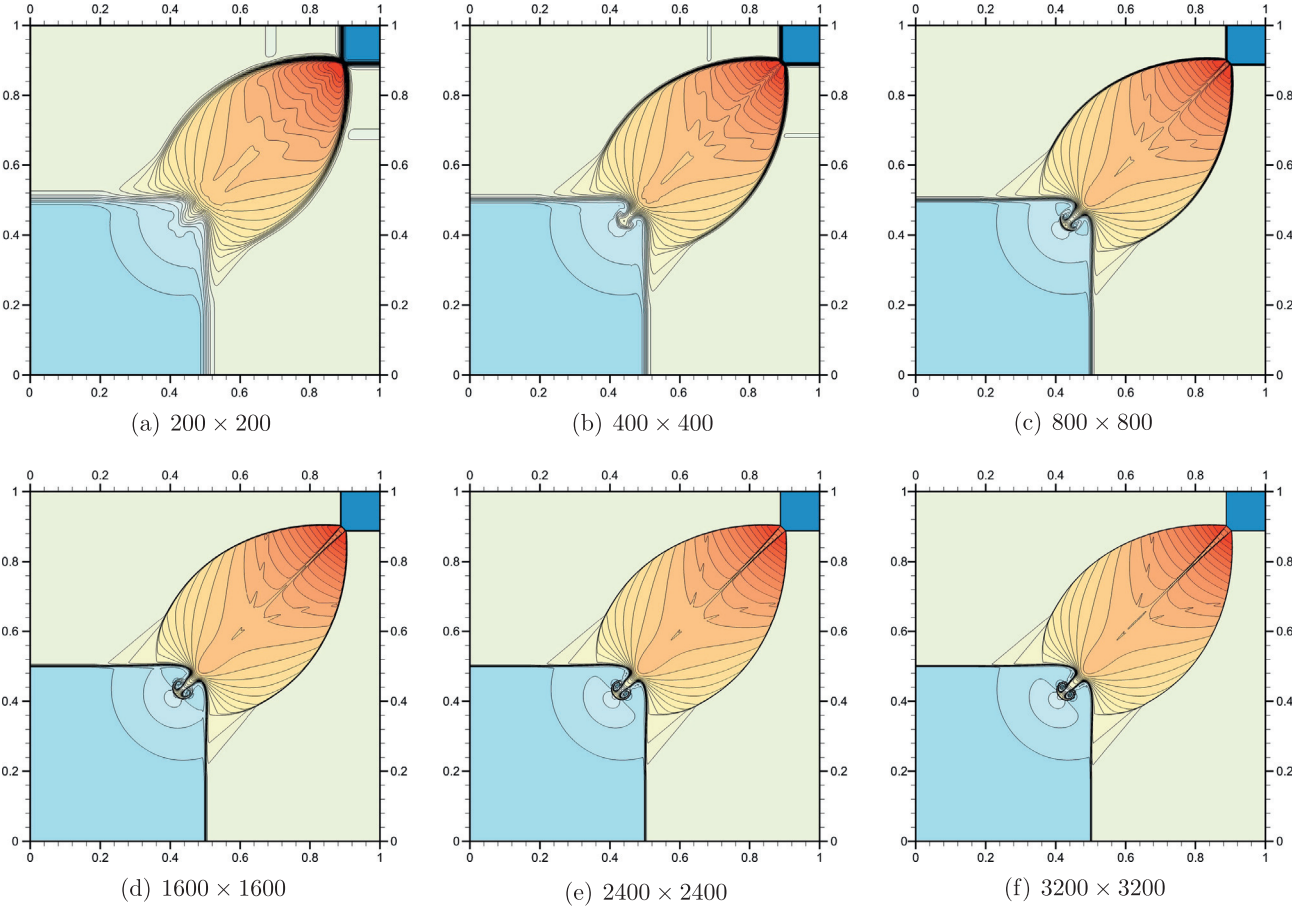


Fig. 6. Configuration 12 of Lax and Liu [19] at time $t = 0.25$. Grid independence study performed by WENO3-S-LFR scheme. The 41 equidistant contour lines are shown between the density levels of 0.55 and 1.65 inclusively.

WENO3-R stands for the third-order WENO reconstruction scheme given by Eqs. (19) and (20). We emphasize here that WENO schemes mostly encountered in literature are used along with the flux-splitting methods [12]. One of the goals in present study is to compare the performance of this reconstruction based WENO scheme with that of the flux-splitting based WENO schemes which will be presented in coming sections.

3.1.3. Rusanov's Riemann solver

Once left and right states are reconstructed the fluxes can be determined based on the maximum local wave propagation speed, Rusanov solver follows [46]

$$F_{i+1/2} = \frac{1}{2} (F^R + F^L) - \frac{c_{i+1/2}}{2} (q_{i+1/2}^R - q_{i+1/2}^L) \quad (23)$$

where F^R is the flux component using the right reconstructed state, $F^R = F(q_{i+1/2}^R)$, and F^L is the flux component using the left reconstructed state, $F^L = F(q_{i+1/2}^L)$, and $c_{i+1/2}$ is the local wave propagation speed which is the maximum absolute value of the eigenvalues corresponding to the Jacobian matrix of F between cells i and $i+1$ given by

$$c_{i+1/2} = \max(r(A_i), r(A_{i+1})) \quad (24)$$

where $r(A)$ represents the spectral radius of convective Jacobian matrix A . For the case of Euler equations, it can be simply written as $r(A) = \max(|u|, |u-a|, |u+a|)$. Thus, the wave propagation speed can be rewritten in the following form

$$c_{i+1/2} = \max(|u|_i, |u-a|_i, |u+a|_i, |u|_{i+1}, |u-a|_{i+1}, |u+a|_{i+1}) \quad (25)$$

The above flux calculation is sometimes referred to as local Lax-Friedrichs flux [20,47,48]. There are other possibilities for estimating the wave propagation speed. For example, one possible way is to use the Roe average between the left and right states and get the spectral radius of this averaged state.

3.1.4. Roe's Riemann solver

According to the Godunov theorem [49], for a hyperbolic system of equations, if the Jacobian matrix of the flux vector is constant (i.e., if A is constant), the exact values of fluxes at the interfaces can be computed by

$$F_{i+1/2} = \frac{1}{2} (F^R + F^L) - \frac{1}{2} R |A| L (q_{i+1/2}^R - q_{i+1/2}^L) \quad (26)$$

where $|A|$ is the diagonal matrix consisted of the absolute values of eigenvalues. In the system of Euler equations, however, the Jacobian matrix A is not constant (i.e., $A = A(q)$). The Roe solver [10], is an approximate Riemann solver based around the Godunov scheme and involves finding an estimate for the interface numerical flux as follows

$$F_{i+1/2} = \frac{1}{2} (F^R + F^L) - \frac{1}{2} \tilde{R} |\tilde{A}| \tilde{L} (q_{i+1/2}^R - q_{i+1/2}^L) \quad (27)$$

where the tilde represents the Roe average (i.e., a density weighted average) between the left and right states. Specifically, the eigen-system matrices can be computed from the density averaged values given by

$$\begin{aligned}\tilde{\rho} &= \frac{\rho_R \sqrt{\rho_R} + \rho_L \sqrt{\rho_L}}{\sqrt{\rho_R} + \sqrt{\rho_L}}, \quad \tilde{u} = \frac{u_R \sqrt{\rho_R} + u_L \sqrt{\rho_L}}{\sqrt{\rho_R} + \sqrt{\rho_L}}, \\ \tilde{v} &= \frac{v_R \sqrt{\rho_R} + v_L \sqrt{\rho_L}}{\sqrt{\rho_R} + \sqrt{\rho_L}}, \quad \tilde{e} = \frac{e_R \sqrt{\rho_R} + e_L \sqrt{\rho_L}}{\sqrt{\rho_R} + \sqrt{\rho_L}}\end{aligned}\quad (28)$$

with the use of the state equations given by Eq. (2), where the left and right states are available to us from the reconstruction formulas given in previous sections. It is realized that the stationary expansion shocks are not dissipated appropriately by this method. Harten [1] proposed the following remedy to fix the entropy in

the expansion shocks. To fix the entropy, the Roe averaged eigenvalues are replaced by

$$|\tilde{\lambda}_i| = \begin{cases} |\tilde{\lambda}_i|, & \text{if } |\tilde{\lambda}_i| \geq 2\varepsilon\tilde{a} \\ \tilde{\lambda}_i^2/(4\varepsilon\tilde{a}) + \varepsilon\tilde{a}, & \text{if } |\tilde{\lambda}_i| < 2\varepsilon\tilde{a} \end{cases} \quad (29)$$

where \tilde{a} is the speed of the sound at averaged state. Here, $\tilde{\lambda}_1 = \tilde{\lambda}_2 = \tilde{u}$, $\tilde{\lambda}_3 = \tilde{u} + \tilde{a}$, and $\tilde{\lambda}_4 = \tilde{u} - \tilde{a}$ are the components of the diagonal matrix Λ . Here, ε is a small positive number and is typically chosen as $\varepsilon = 0.1$ in our computations. Although it is not included in our computations, the Lax–Friedrichs flux with wave

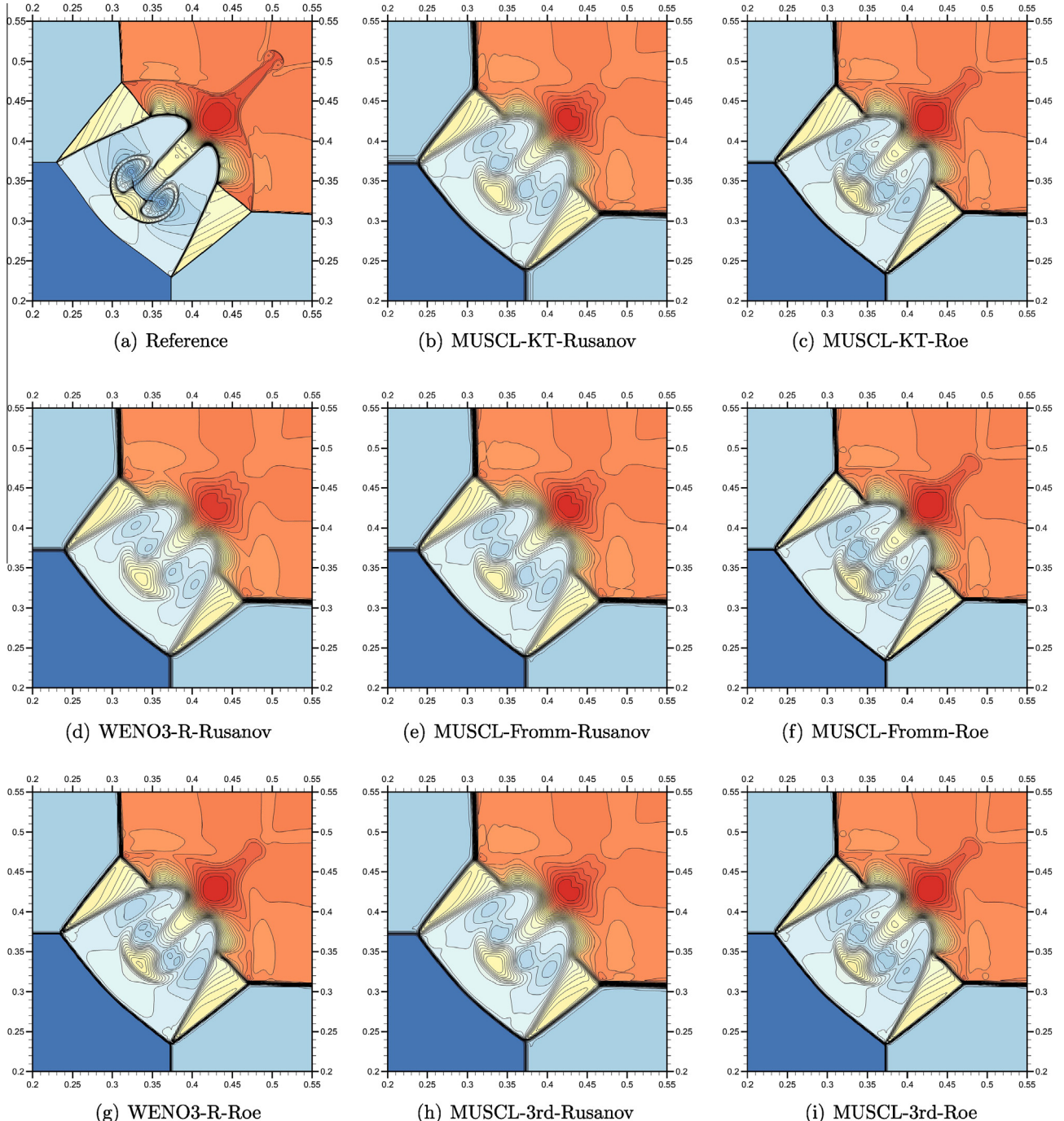


Fig. 7. Configuration 3 of Lax and Liu [19] at time $t = 0.3$. The effects of Riemann solvers for reconstruction schemes using the resolution of 400×400 . In all figures, the contour levels are identical to the reference solution.

propagation speed based on the Roe averages can also be recovered from Eq. (27) when we replace the eigenvalues with

$$|\tilde{\lambda}_i| = \max\left(\tilde{\lambda}_i, \max(\tilde{\lambda}_1, \tilde{\lambda}_2, \tilde{\lambda}_3, \tilde{\lambda}_4)\right). \quad (30)$$

3.2. Flux-splitting WENO schemes

In the following, we explain several implementations for the weighted essentially non-oscillatory (WENO) scheme which can be considered one of the state-of-art shock capturing methods [8,12,50]. As we discussed earlier, we can generally classify the

state-of-art shock capturing schemes as (i) reconstruction based approaches and (ii) flux-splitting based approaches. Variants of WENO schemes can be constructed in both procedures. In the first approach, WENO reconstruction can be utilized to construct left and right states at the cell boundaries from the solution available at the cell centers, and a Riemann solver can be used to find fluxes at the cell boundaries [45]. This procedure is explained in previous section by using the third-order reconstruction scheme. In the second approach, depending on the direction in which the information is propagating, flux-splitting can be first performed to obtain positive and negative fluxes, and then WENO reconstruction can be used to compute both fluxes at the cell boundaries [12]. In this

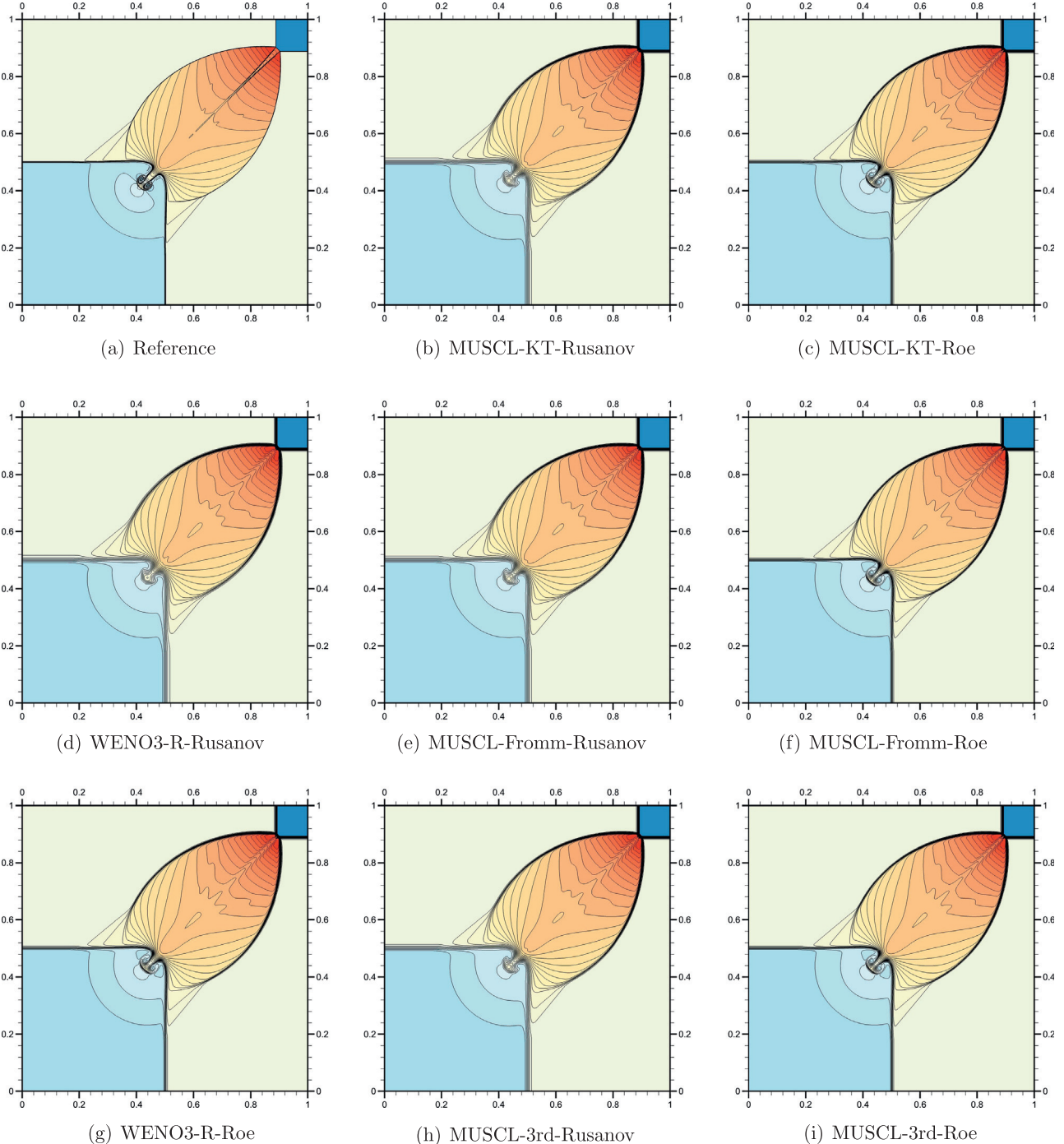


Fig. 8. Configuration 12 of Lax and Liu [19] at time $t = 0.25$. The effects of Riemann solvers for reconstruction schemes using the resolution of 400×400 . In all figures, the contour levels are identical to the reference solution.

Table 1

Computed L^2 norms of density fields, $\|L^2(\rho)\|$, for the solutions obtained by various Riemann solvers and reconstruction schemes on a grid resolution of 400^2 . Reference solutions are obtained by the MUSCL-KT scheme on a grid resolution of 3200^2 .

Scheme	Configuration 3	Configuration 12
MUSCL-KT-Rusanov	1.4931E-3	2.6209E-4
MUSCL-KT-Roe	8.8567E-4	2.1643E-4
MUSCL-Fromm-Rusanov	1.5045E-3	2.6076E-4
MUSCL-Fromm-Roe	8.9596E-4	2.1556E-4
MUSCL-3rd-Rusanov	1.5055E-3	2.6101E-4
MUSCL-3rd-Roe	8.9978E-4	2.1588E-4
WENO3-R-Rusanov	1.7122E-3	2.9168E-4
WENO3-R-Roe	1.0512E-3	2.3633E-4

section, we focus the second approach testing several forms of the splitting procedures.

Depending on the direction in which the information is propagating, flux vector splitting framework can be used for constructing high-order shock capturing schemes. The basic idea of flux-splitting is to decompose the flux vectors into two parts

$$F = F^+ + F^-, \quad G = G^+ + G^- \quad (31)$$

and the WENO reconstruction procedures are then applied to the both positive and negative parts separately which will be presented in the following sections. Several flux vector splitting methods can be used to decompose the fluxes. In this study, we only focus the

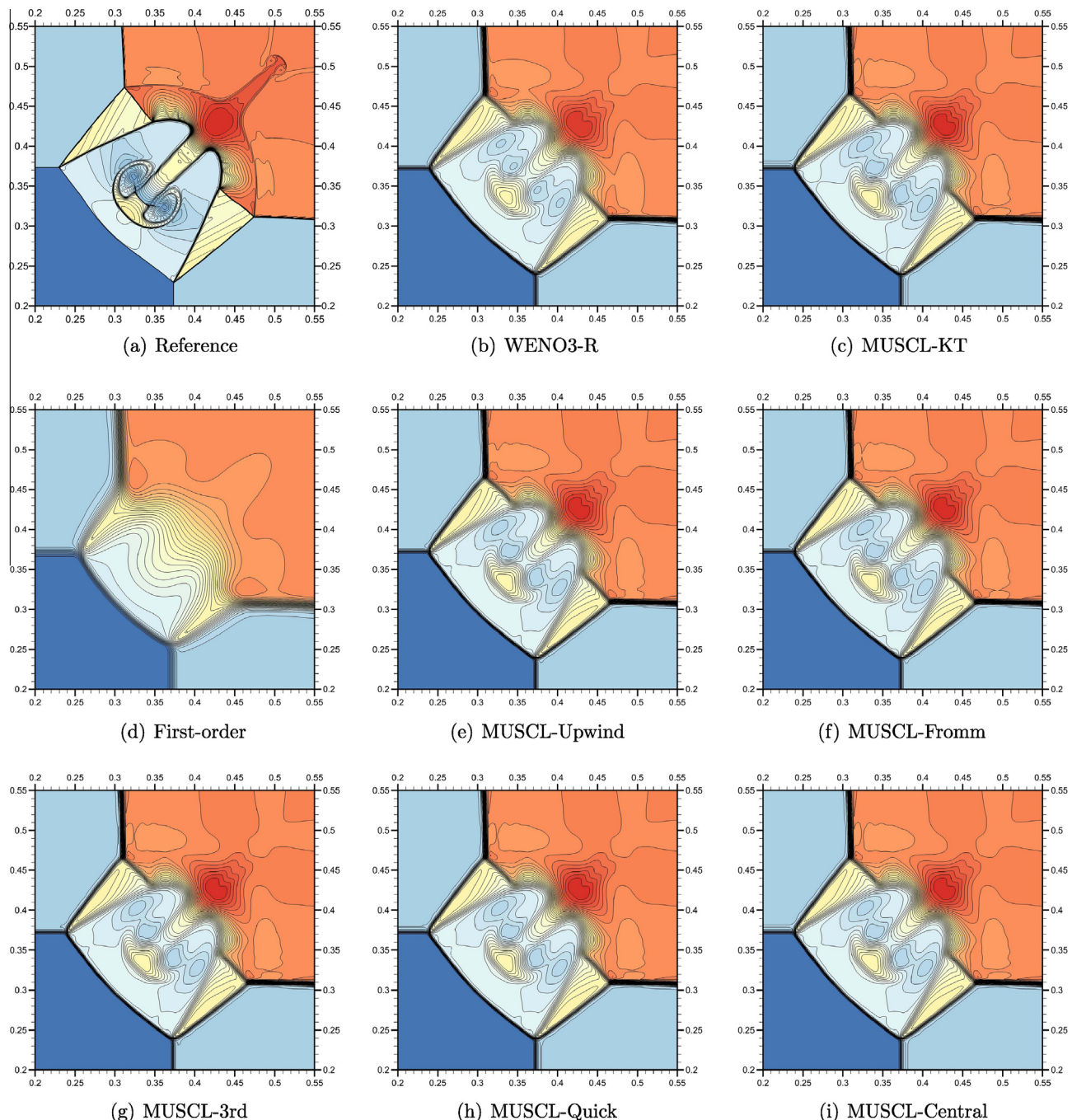


Fig. 9. Configuration 3 of Lax and Liu [19] at time $t = 0.3$. Comparison of the reconstruction schemes with Rusanov solver using the resolution of 400×400 . In all figures, the contour levels are identical to the reference solution.

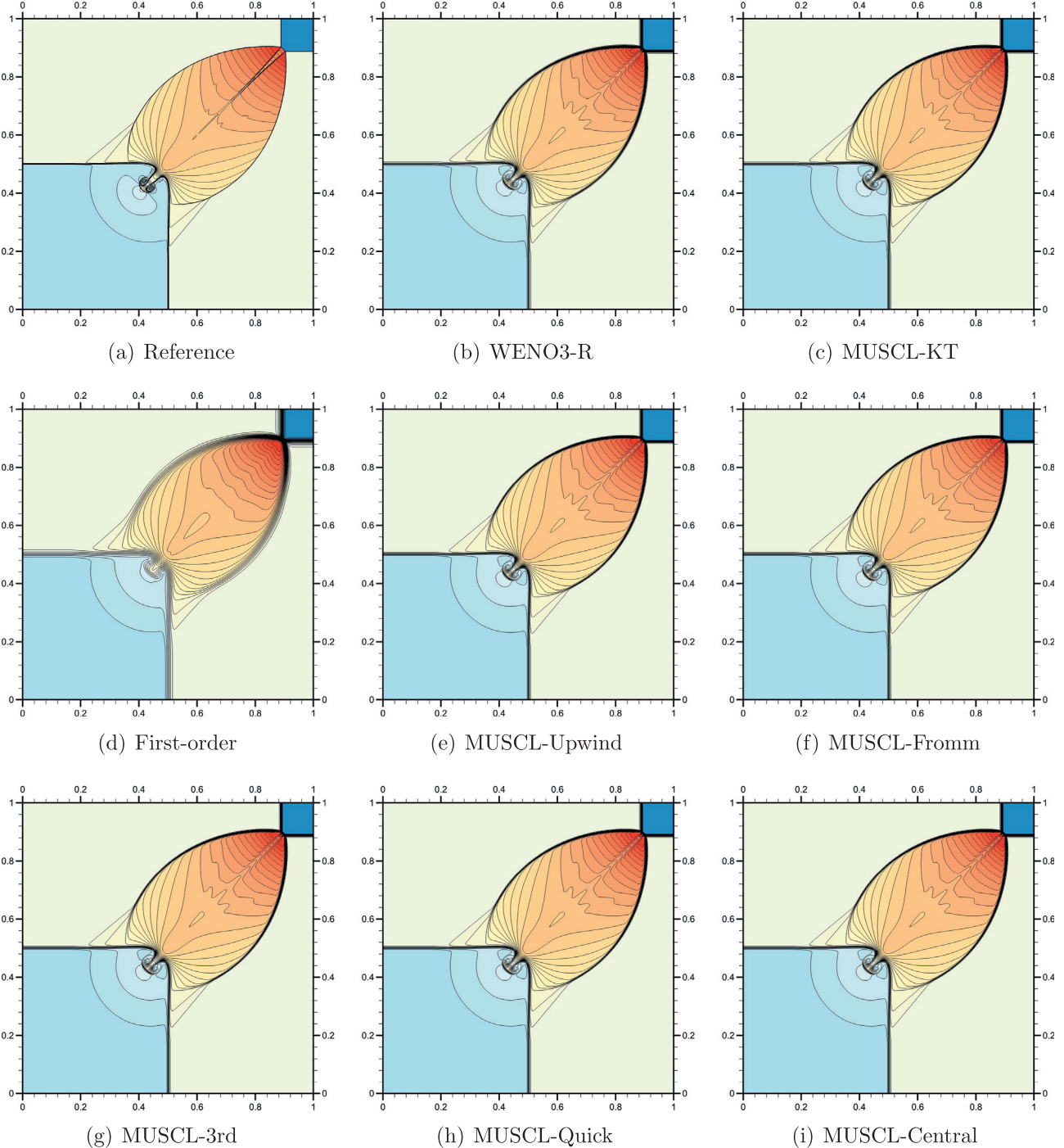


Fig. 10. Configuration 12 of Lax and Liu [19] at time $t = 0.25$. Comparison of the reconstruction schemes with Rusanov solver using the resolution of 400×400 . In all figures, the contour levels are identical to the reference solution.

local splitting procedures with their simplicity. More complex splitting procedures can be found in literature (e.g., using the characteristics based transformations on the selective stencils in a close neighborhood of the cell [51–53]).

Using the definition of Eq. (31), the semi-discrete form of the Euler equations given in Eq. (3) can be rewritten as

$$\frac{dq_{ij}}{dt} + \frac{1}{\Delta x} (F_{i+1/2,j}^+ - F_{i-1/2,j}^-) + \frac{1}{\Delta y} (G_{ij+1/2}^+ - G_{ij-1/2}^-) + \frac{1}{\Delta x} (F_{i+1/2,j}^- - F_{i-1/2,j}^+) + \frac{1}{\Delta y} (G_{ij+1/2}^- - G_{ij-1/2}^+) = 0 \quad (32)$$

where the positive and negative fluxes at the cell boundaries are computed using the WENO reconstruction procedures from the cell centered valued fluxes. Similar to our previous treatments, we will omit the spatial index which is not in the direction of the action. We only present the schemes showing the procedures in x -direction, however, the same procedures are applied in y -direction.

3.2.1. The third-order WENO reconstruction

To compute fluxes at the cell boundaries, the third-order WENO reconstruction procedure in x -direction becomes

$$F_{i+1/2}^+ = \frac{w_1^+}{2} (-F_{i-1}^+ + 3F_i^+) + \frac{w_2^+}{2} (F_i^+ + F_{i+1}^+) \quad (33)$$

$$F_{i-1/2}^- = \frac{w_1^-}{2} (F_{i-1}^- + F_i^-) + \frac{w_2^-}{2} (3F_i^- - F_{i+1}^-) \quad (34)$$

where nonlinear weights are defined as

$$w_1^\pm = \frac{\alpha_1^\pm}{\alpha_1^\pm + \alpha_2^\pm} \quad w_2^\pm = \frac{\alpha_2^\pm}{\alpha_1^\pm + \alpha_2^\pm} \quad (35)$$

and

$$\alpha_1^\pm = \frac{d_1^\pm}{(\beta_1^\pm + \epsilon)^2} \quad \alpha_2^\pm = \frac{d_2^\pm}{(\beta_2^\pm + \epsilon)^2} \quad (36)$$

Table 2

Computed L^2 norms of density fields, $\|L^2(\rho)\|$, for the solutions obtained by various MUSCL reconstruction schemes on a grid resolution of 400^2 using the Rusanov solver with the Van Albada flux-limiter. Results from the WENO3 reconstruction and the first-order reconstruction given by Eq. (7) are also included. Reference solutions are obtained by the MUSCL-KT scheme on a grid resolution of 3200^2 .

Scheme	Configuration 3	Configuration 12
First-order	4.6460E-3	1.0998E-3
MUSCL-KT	1.4931E-3	2.6209E-4
MUSCL-Upwind ($\kappa = -1$)	1.5013E-3	2.6008E-4
MUSCL-Fromm ($\kappa = 0$)	1.5045E-3	2.6076E-4
MUSCL-3rd ($\kappa = 1/3$)	1.5055E-3	2.6101E-4
MUSCL-Quick ($\kappa = 1/2$)	1.5060E-4	2.6159E-4
MUSCL-Central ($\kappa = 1$)	1.5070E-4	2.6164E-4
WENO3-R	1.7122E-3	2.9168E-4

in which $\epsilon = 10^{-6}$ is used to avoid denominators become zero and the smoothness indicators are defined as

$$\beta_1^\pm = (F_i^\pm - F_{i-1}^\pm)^2, \quad \beta_2^\pm = (F_{i+1}^\pm - F_i^\pm)^2 \quad (37)$$

where linear weighting coefficients are $d_1^+ = 1/3$ and $d_2^+ = 2/3$ in the positive fluxes, and $d_1^- = 2/3$ and $d_2^- = 1/3$ in the negative fluxes.

3.2.2. The fifth-order WENO reconstruction

Similarly, using total 7 point stencil, the fifth-order WENO reconstruction procedure in x -direction becomes

$$F_{i+1/2}^+ = \frac{w_1^+}{6} (2F_{i-2}^+ - 7F_{i-1}^+ + 11F_i^+) + \frac{w_2^+}{6} (-F_{i-1}^+ + 5F_i^+ + 2F_{i+1}^+) + \frac{w_3^+}{6} (2F_i^+ + 5F_{i+1}^+ - F_{i+2}^+) \quad (38)$$

$$F_{i-1/2}^- = \frac{w_1^-}{6} (-F_{i-2}^- + 5F_{i-1}^- + 2F_i^-) + \frac{w_2^-}{6} (2F_{i-1}^- + 5F_i^- - F_{i+1}^-) + \frac{w_3^-}{6} (11F_i^- - 7F_{i+1}^- + 2F_{i+2}^-) \quad (39)$$

where nonlinear weights are defined as

$$w_1^\pm = \frac{\alpha_1^\pm}{\alpha_1^\pm + \alpha_2^\pm + \alpha_3^\pm} \quad w_2^\pm = \frac{\alpha_2^\pm}{\alpha_1^\pm + \alpha_2^\pm + \alpha_3^\pm} \quad w_3^\pm = \frac{\alpha_3^\pm}{\alpha_1^\pm + \alpha_2^\pm + \alpha_3^\pm} \quad (40)$$

and

$$\alpha_1^\pm = \frac{d_1^\pm}{(\beta_1^\pm + \epsilon)^2} \quad \alpha_2^\pm = \frac{d_2^\pm}{(\beta_2^\pm + \epsilon)^2} \quad \alpha_3^\pm = \frac{d_3^\pm}{(\beta_3^\pm + \epsilon)^2} \quad (41)$$

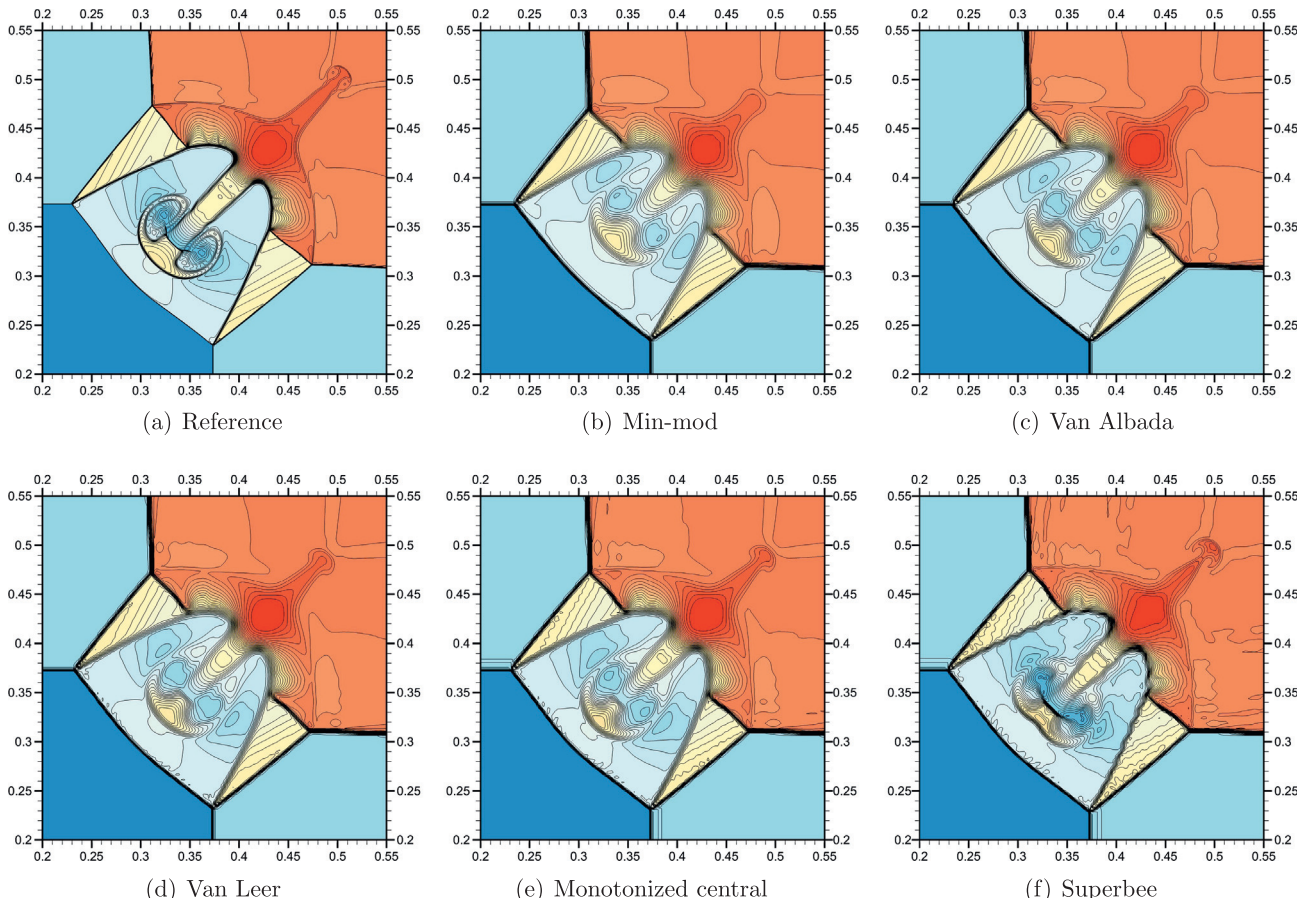


Fig. 11. Configuration 3 of Lax and Liu [19] at time $t = 0.3$. The effects of flux-limiters for the MUSCL-3rd order reconstruction scheme with the Roe solver using the resolution of 400×400 . In all figures, the contour levels are identical to the reference solution.

in which $\epsilon = 10^{-6}$ is used to avoid denominators become zero and the linear weighting coefficients are $d_1^+ = 1/10$, $d_2^+ = 6/10$, and $d_3^+ = 3/10$ in the positive fluxes, and $d_1^- = 3/10$, $d_2^- = 6/10$, and $d_3^- = 1/10$ in the negative fluxes. The smoothness indicators in the stencils are defined as [12]:

$$\beta_1^\pm = \frac{13}{12} (F_{i-2}^\pm - 2F_{i-1}^\pm + F_i^\pm)^2 + \frac{1}{4} (F_{i-2}^\pm - 4F_{i-1}^\pm + 3F_i^\pm)^2 \quad (42)$$

$$\beta_2^\pm = \frac{13}{12} (F_{i-1}^\pm - 2F_i^\pm + F_{i+1}^\pm)^2 + \frac{1}{4} (F_{i-1}^\pm - F_{i+1}^\pm)^2 \quad (43)$$

$$\beta_3^\pm = \frac{13}{12} (F_i^\pm - 2F_{i+1}^\pm + F_{i+2}^\pm)^2 + \frac{1}{4} (3F_i^\pm - 4F_{i+1}^\pm + F_{i+2}^\pm)^2. \quad (44)$$

3.2.3. Lax–Friedrichs splitting

One of the simplest, albeit more dissipative, splitting methods is local Lax–Friedrichs flux-splitting which can be written as

$$F^\pm = \frac{1}{2} \left(F \pm \frac{\partial F}{\partial q} q \right), \quad G^\pm = \frac{1}{2} \left(G \pm \frac{\partial G}{\partial q} q \right) \quad (45)$$

which can be written as

$$F^\pm = \frac{1}{2} (F \pm R | A | Lq), \quad G^\pm = \frac{1}{2} (G \pm T | \Psi | Sq) \quad (46)$$

In this study, WENO-S-LF stands for the WENO scheme with the flux-splitting given by Eq. (46). The Lax–Friedrichs splitting given in Eq. (46) can also be further simplified to the

$$F^\pm = \frac{1}{2} (F \pm \alpha q), \quad G^\pm = \frac{1}{2} (G \pm \beta q) \quad (47)$$

where α and β are the maximum values of absolute values of local eigenvalues, explicitly given as $\alpha = \max(|u|, |u+a|, |u-a|)$, and $\beta = \max(|v|, |v+a|, |v-a|)$. This version of the Lax–Friedrichs flux-splitting is computationally more efficient than the splitting procedure given by Eq. (46) and it is quite similar the Rusanov solver introduced earlier [47,48]. Therefore, it is sometimes referred to as Rusanov flux-splitting. Therefore, to highlight the difference from the Lax–Friedrichs splitting given by Eq. (46), in this work, we denote the WENO scheme with the flux-splitting given by Eq. (47) as WENO-S-LFR.

3.2.4. Steger and Warming splitting

Steger and Warming [21] developed the following flux-splitting procedure based on a eigenvalue decomposition

$$\lambda_i = \lambda_i^+ + \lambda_i^-, \quad \psi_i = \psi_i^+ + \psi_i^- \quad (48)$$

where λ_i and ψ_i are respectively eigenvalues of A and B matrices. Then, the split-fluxes become

$$F^\pm = \frac{\rho}{2\gamma} \begin{pmatrix} \lambda_4^\pm + 2(\gamma-1)\lambda_1^\pm + \lambda_3^\pm \\ (u-a)\lambda_4^\pm + 2(\gamma-1)u\lambda_1^\pm + (u+a)\lambda_3^\pm \\ v\lambda_4^\pm + 2(\gamma-1)v\lambda_1^\pm + v\lambda_3^\pm \\ (H-ua)\lambda_4^\pm + 2\phi^2\lambda_1^\pm + (H+ua)\lambda_3^\pm \end{pmatrix}$$

$$G^\pm = \frac{\rho}{2\gamma} \begin{pmatrix} \psi_4^\pm + 2(\gamma-1)\psi_1^\pm + \psi_3^\pm \\ u\psi_4^\pm + 2(\gamma-1)u\psi_1^\pm + u\psi_3^\pm \\ (\nu-a)\psi_4^\pm + 2(\gamma-1)\nu\psi_1^\pm + (\nu+a)\psi_3^\pm \\ (H-\nu a)\psi_4^\pm + 2\phi^2\psi_1^\pm + (H+\nu a)\psi_3^\pm \end{pmatrix}$$

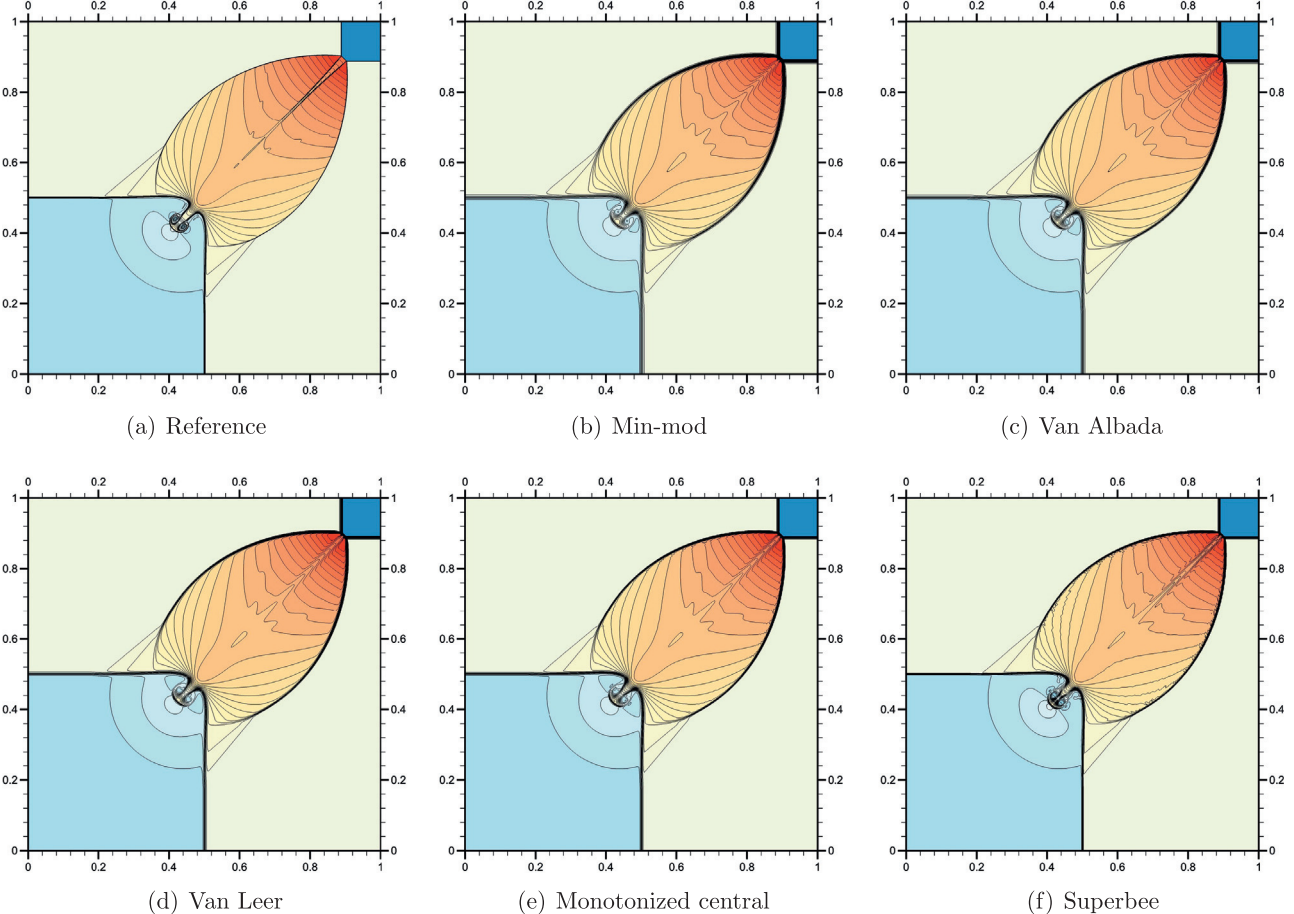


Fig. 12. Configuration 12 of Lax and Liu [19] at time $t = 0.25$. The effects of flux-limiters for the MUSCL-3rd order reconstruction scheme with the Roe solver using the resolution of 400×400 . In all figures, the contour levels are identical to the reference solution.

where $\phi^2 = \frac{1}{2}(\gamma - 1)(u^2 + v^2)$; the eigenvalues of A are $\lambda_1 = \lambda_2 = u$, $\lambda_3 = u + a$, and $\lambda_4 = u - a$; and the eigenvalues of B are $\psi_1 = \psi_2 = v$, $\psi_3 = v + a$, and $\psi_4 = v - a$. The split fluxes are continuous but not differentiable due to the sign change in Eq. (48). This can lead to spurious numerical errors near the stagnation and sonic points. Similar to remedy for the entropy fix in Roe solver, the eigenvalues are blended smoothly into their zero's [54]

$$\lambda_i^\pm = \frac{1}{2} \left(\lambda_i \pm \sqrt{\lambda_i^2 + \varepsilon^2 a^2} \right), \quad \psi_i^\pm = \frac{1}{2} \left(\psi_i \pm \sqrt{\psi_i^2 + \varepsilon^2 a^2} \right) \quad (49)$$

where it is typical to choose the $\varepsilon = 0.1$. The resulting joint solver is called as WENO-S-SW.

3.2.5. Van Leer splitting

Van Leer [22] developed a flux-splitting procedure in which he imposed a requirement that $\frac{\partial F^\pm}{\partial q}$ and $\frac{\partial G^\pm}{\partial q}$ must be continuous function of directional Mach numbers defined as $M_x = u/a$ and $M_y = v/a$. Then the split procedure follows: $F^+ = F$ and $F^- = 0$ if $M_x \geq 1$; $F^- = F$ and $F^+ = 0$ if $M_x \leq 1$. When flow speed is $0 < M_x < 1$, the positive-flux is computed by

$$F^+ = \frac{1}{4} \rho a (M_x + 1)^2 \begin{pmatrix} 1 \\ u + \frac{2a-u}{\gamma} \\ v \\ \frac{2a^2-(\gamma-1)u^2+2(\gamma-1)au}{\gamma^2-1} + \frac{u^2+v^2}{2} \end{pmatrix} \quad (50)$$

and negative-flux component becomes $F^- = F - F^+$. For $-1 < M_x < 0$, the negative-flux is computed according to

$$F^- = -\frac{1}{4} \rho a (M_x - 1)^2 \begin{pmatrix} 1 \\ u - \frac{2a+u}{\gamma} \\ v \\ \frac{2a^2-(\gamma-1)u^2-2(\gamma-1)au}{\gamma^2-1} + \frac{u^2+v^2}{2} \end{pmatrix} \quad (51)$$

and the remaining positive-flux component is computed by $F^+ = F - F^-$. Similarly, the splitting can be written in y direction as

$$G^+ = \frac{1}{4} \rho a (M_y + 1)^2 \begin{pmatrix} 1 \\ u \\ v + \frac{2a-v}{\gamma} \\ \frac{2a^2-(\gamma-1)v^2+2(\gamma-1)av}{\gamma^2-1} + \frac{u^2+v^2}{2} \end{pmatrix} \quad (52)$$

$$G^- = -\frac{1}{4} \rho a (M_y - 1)^2 \begin{pmatrix} 1 \\ u \\ v - \frac{2a+v}{\gamma} \\ \frac{2a^2-(\gamma-1)v^2-2(\gamma-1)av}{\gamma^2-1} + \frac{u^2+v^2}{2} \end{pmatrix}. \quad (53)$$

The resulting joint solver is called as WENO-S-VL.

4. Results

The main goal of this section is to test and evaluate the joint solvers introduced in Section 3 in the numerical simulation of the two-dimensional Euler equations. In order to analyze the behavior of these schemes various test problems described by Lax and Liu [19] having different properties including shock and

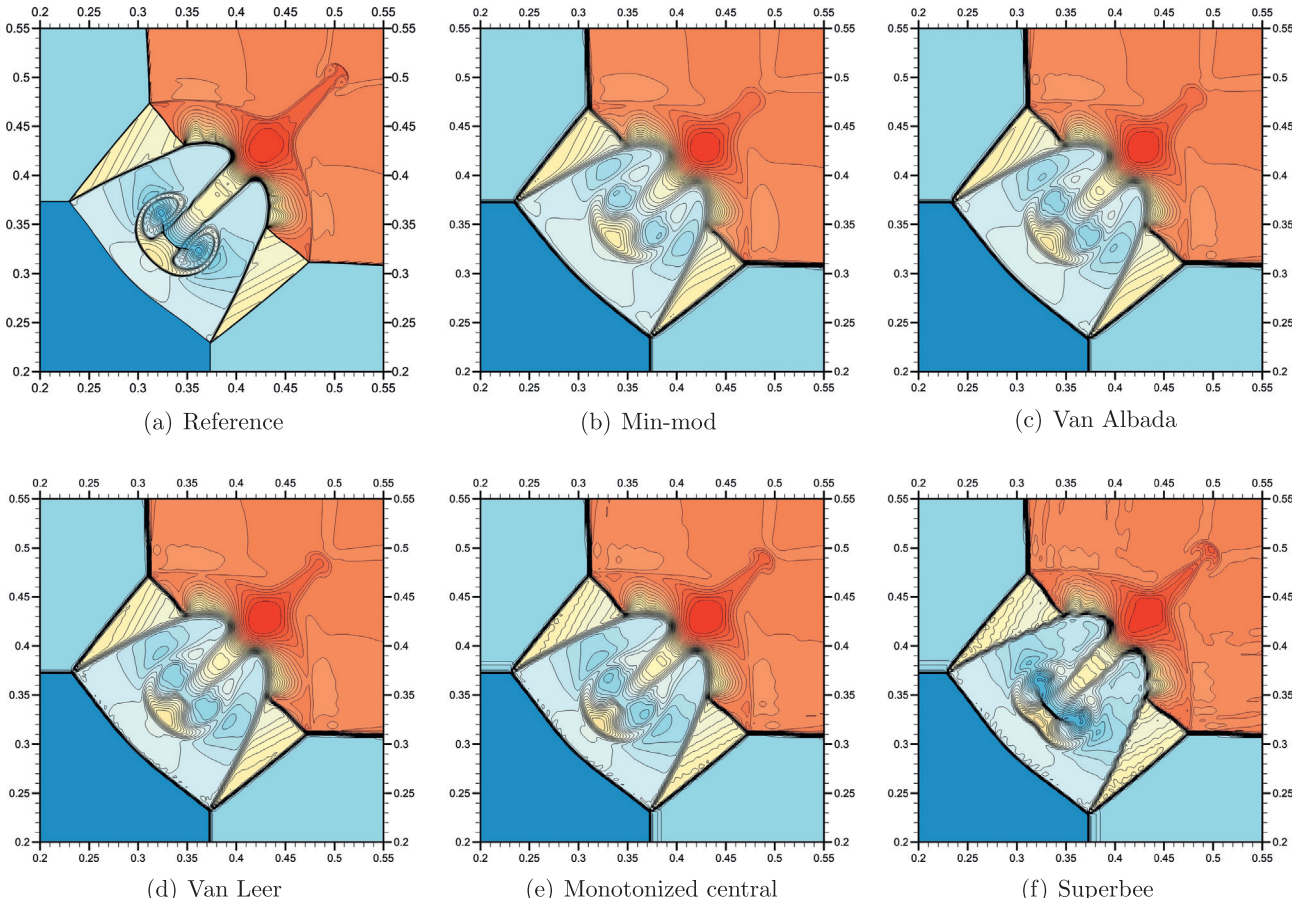


Fig. 13. Configuration 3 of Lax and Liu [19] at time $t = 0.3$. The effects of flux-limiters for the MUSCL-KT reconstruction scheme with the Roe solver using the resolution of 400×400 . In all figures, the contour levels are identical to the reference solution.

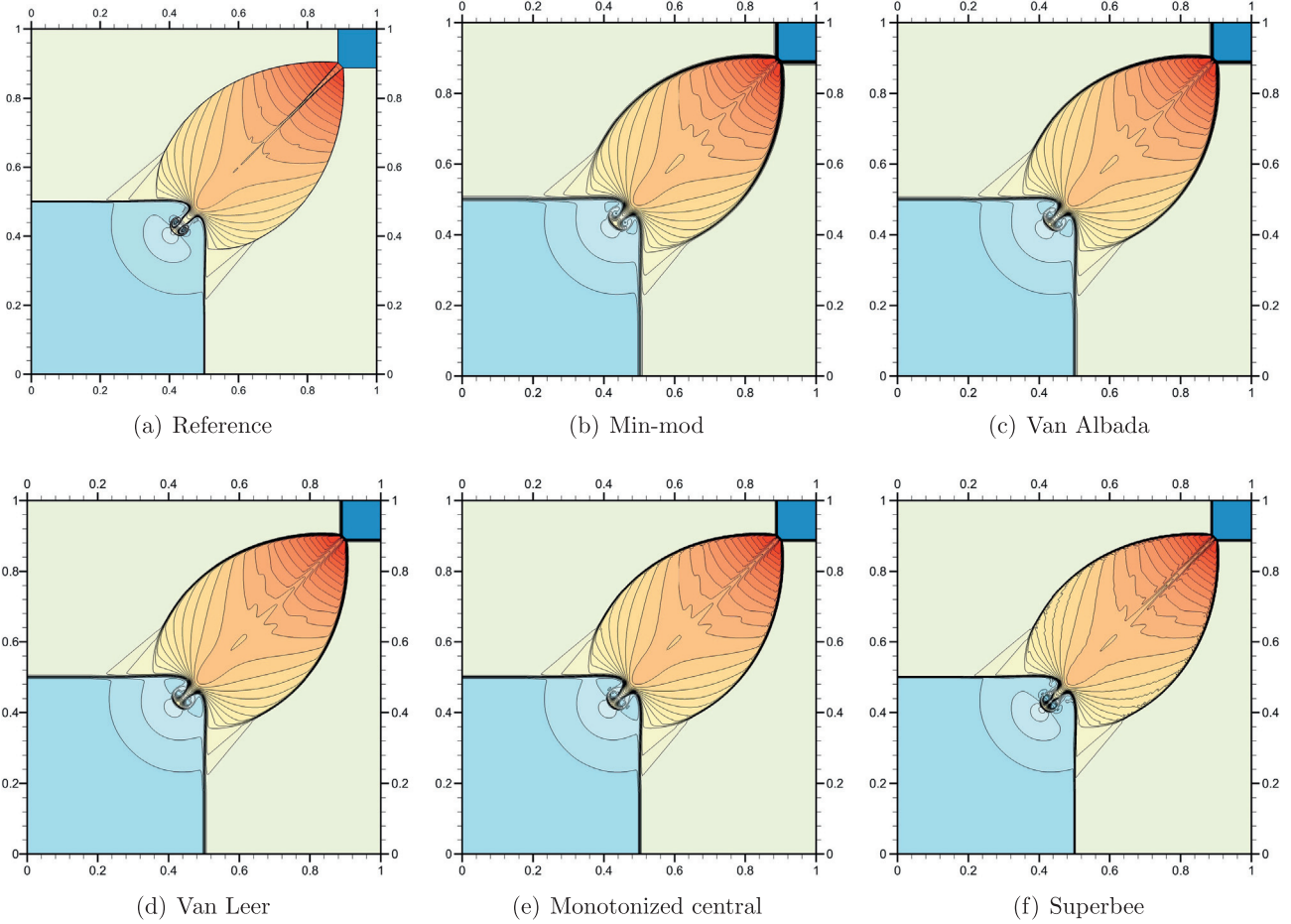


Fig. 14. Configuration 12 of Lax and Liu [19] at time $t = 0.25$. The effects of flux-limiters for the MUSCL-KT reconstruction scheme with the Roe solver using the resolution of 400×400 . In all figures, the contour levels are identical to the reference solution.

rarefaction waves as well as contact discontinuities. In this study, we use six of these benchmark problems by using a ratio of specific heats, $\gamma = 1.4$. Initial configurations in each quadrant are shown in

Fig. 2 for completeness. The interested reader is referred to their archival manuscript for the details of the wave structures of each configuration for these benchmark test problems.

4.1. The performance of five-point stencil high-resolution schemes

This section investigates the performance characteristics of five-point stencil high-resolution schemes for hyperbolic conservation laws by solving two-dimensional Riemann problems for the Euler equations. Several variants of MUSCL and WENO reconstruction and flux-splitting procedures are considered and compared for their effectiveness. We demonstrate our results for solving two test problems: (i) Configuration 3 of Lax and Liu [19] involving four shocks, and (ii) Configuration 12 of Lax and Liu [19] involving two shocks and two contact discontinuities. First, a grid independence study is performed by the MUSCL-KT reconstruction scheme using the Van Albada flux limiter. As shown in **Fig. 3** for various resolutions from 200^2 to 3200^2 at time $t = 0.3$, the four shocks structure in Configuration 3 produces a narrow jet, which becomes more clear in higher resolutions. The field snapshots shown in **Fig. 3** demonstrate 41 equidistant contour lines between the density levels of 0.2 and 1.7 inclusively. Similarly, **Fig. 4** illustrates results for Configuration 12 in which 41 equidistant contour lines between the density levels of 0.55 and 1.65 are plotted at time $t = 0.25$. As we can see, the presence of thinner and thinner discontinuous layers as the flow field evolves in time is not fully captured by low grid resolution representations. **Fig. 5** and **Fig. 6** demonstrate the same grid refinement analysis by using the third-order

Table 3

Computed L^2 norms of density fields, $\|L^2(\rho)\|$, for the solutions obtained by various flux-limiters using the underlying MUSCL-3rd reconstruction scheme with Roe's approximate Riemann solver on a grid resolution of 400^2 . Reference solutions are obtained by the MUSCL-KT scheme on a grid resolution of 3200^2 .

Flux-limiter	Configuration 3	Configuration 12
Min-mod	1.1803E-3	2.5139E-4
Van Albada	8.9978E-4	2.1588E-4
Van Leer	6.6052E-4	1.8406E-4
Monotonized central	3.6999E-4	1.5300E-4
Superbee	2.5796E-4	8.0691E-4

Table 4

Computed L^2 norms of density fields, $\|L^2(\rho)\|$, for the solutions obtained by various flux-limiters using the underlying MUSCL-KT reconstruction scheme with Roe's approximate Riemann solver on a grid resolution of 400^2 . Reference solutions are obtained by the MUSCL-KT scheme on a grid resolution of 3200^2 .

Flux-limiter	Configuration 3	Configuration 12
Min-mod	1.1803E-3	2.5319E-4
Van Albada	8.8567E-4	2.1643E-4
Van Leer	6.6052E-4	1.8404E-4
Monotonized central	3.6999E-4	1.5300E-4
Superbee	2.5796E-4	8.0691E-4

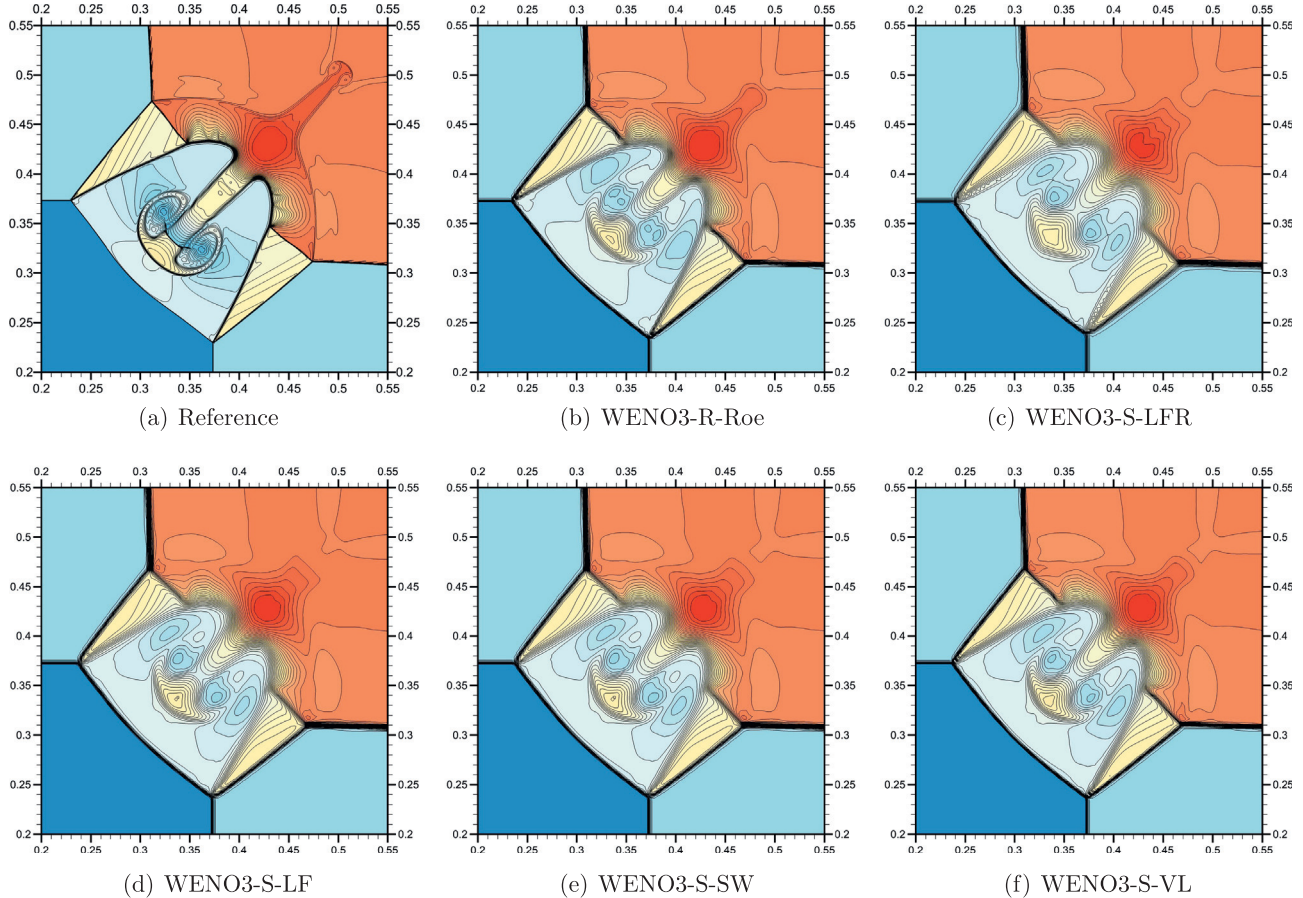


Fig. 15. Configuration 3 of Lax and Liu [19] at time $t = 0.3$. Comparison of flux-splitting schemes using the resolution of 400×400 . In all figures, the contour levels are identical to the reference solution. The reconstruction based WENO scheme with Roe solver, WENO3-R-Roe, is also included for comparison purposes.

WENO scheme with local Lax–Friedrichs–Rusanov flux-splitting, WENO3-S-LFR, in solving the Configuration 3 and Configuration 12 of Lax and Liu [19], respectively. As expected, the sharp non-oscillatory gradients are obtained by increasing resolution. In the following analysis, we use the data obtained by the MUSCL-KT reconstruction scheme on the highest resolution of 3200^2 as a reference solution to our further evaluations.

Although the grid independence studies show that the results depend mostly on the resolution that have been considered, this paper concentrates on the solutions among many variants of the high-order shock capturing schemes to draw numerical assessments on their accuracy. Based on our grid refinement analysis, it should also be highlighted that the development of effective adaptive mesh refinement procedures is crucial to accurate representation of a discontinuity within a smaller grid bandwidth. In this paper, however, we would like to investigate the performance of several high-order joint solvers on a fixed grid system. In the following analysis, the effects of several reconstruction procedures in combination with various Riemann solvers at the cell interfaces are investigated using a resolution of 400^2 . Several variants of flux-limiter based MUSCL reconstruction procedures are compared with the WENO reconstruction procedure which is based on the idea of nonlinear weights with the smoothness indicators.

First, the effects of the selection of Riemann solvers on the accuracy of the reconstruction based solver are systematically investigated for the same test cases. Figs. 7 and 8 compare joint Riemann solvers of Roe and Rusanov with various forms of reconstruction procedures for the Configuration 3 and Configuration 12 of Lax and Liu [19], respectively. The Van Albada flux limiter is used in all the MUSCL reconstruction schemes presented in these figures. Our

comparisons in Figs. 7 and 8 also include several MUSCL reconstruction schemes such as Kurganov and Tadmor, Fromm scheme ($\kappa = 0$), the 3rd-order scheme ($\kappa = 1/3$) as well as the third-order WENO reconstruction. It can be seen that the Roe's approximate Riemann solver produces less dissipative results compared to the Rusanov's approximate Riemann solver. Due to the use of a symmetric flux limiter results are nearly independent of κ for MUSCL schemes. It can also be seen that there are no significant differences between the third-order WENO and MUSCL reconstructions. Our results clearly show that the dissipative character of the Riemann solver is more crucial on the accuracy of the solution process than the selection of the reconstruction procedure. The reason is that the approximate Riemann solvers are highly sensitive to how well a discontinuity is aligned with the underlying grid of the problem. For our cases in which the grid is not aligned with the discontinuity, cross coupling between the Riemann problems in the different directions introduces numerical dissipation error that scales directly with the cell

Table 5

Computed L^2 norms of density fields, $\|L^2(\rho)\|$, for the solutions obtained by various flux-splitting schemes on a grid resolution of 400^2 . The results obtained by the same stencil reconstruction based schemes with Rusanov's and Roe's approximate Riemann solvers are also included. Reference solutions are obtained by the MUSCL-KT scheme on a grid resolution of 3200^2 .

Scheme	Configuration 3	Configuration 12
WENO3-S-LFR	1.5391E-3	3.1298E-4
WENO3-S-LF	1.4361E-4	2.8434E-4
WENO3-S-SW	1.4987E-4	2.9020E-4
WENO3-S-VL	1.2953E-4	2.6530E-4
WENO3-R-Rusanov	1.7122E-3	2.9168E-4
WENO3-R-Roe	1.0512E-3	2.3633E-4

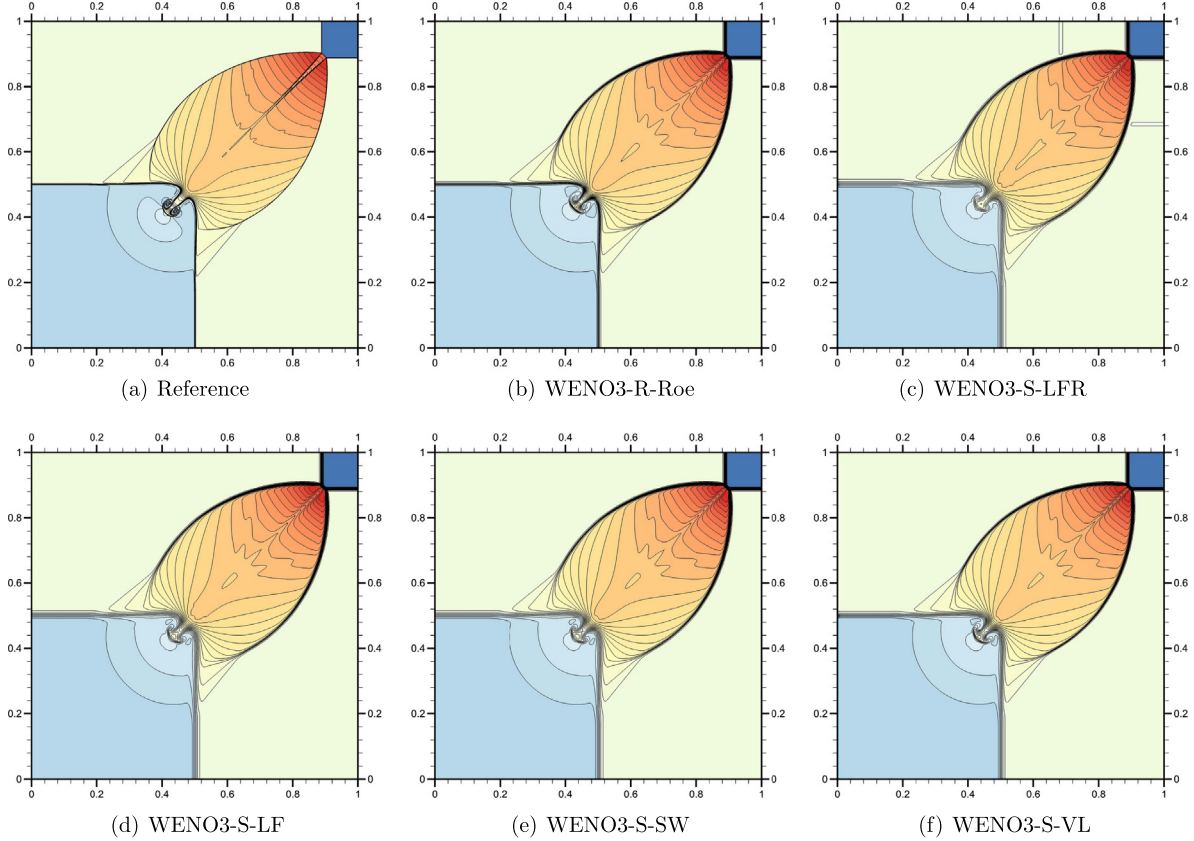


Fig. 16. Configuration 12 of Lax and Liu [19] at time $t = 0.25$. Comparison of flux-splitting schemes using the resolution of 400×400 . In all figures, the contour levels are identical to the reference solution. The reconstruction based WENO scheme with Roe solver, WENO3-R-Roe, is also included for comparison purposes.

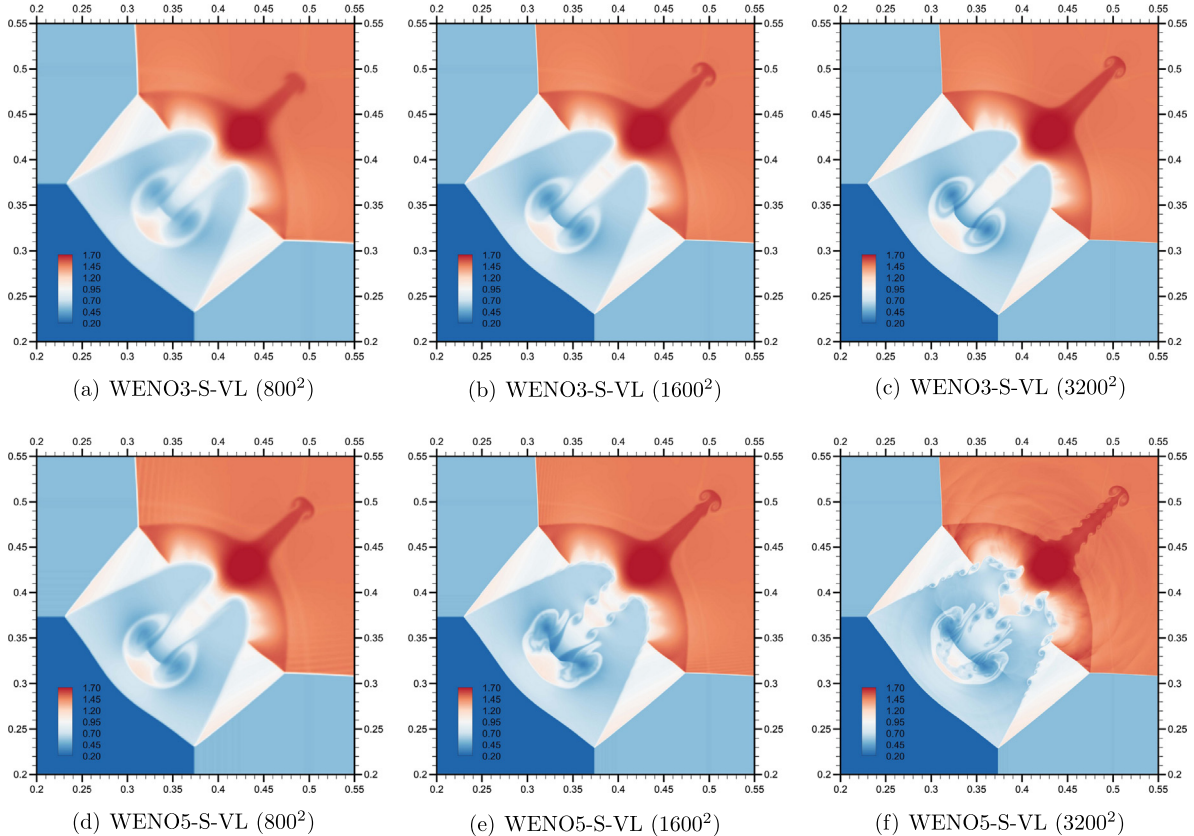


Fig. 17. Configuration 3 of Lax and Liu [19] at time $t = 0.3$. Density fields obtained by using the WENO3 and WENO5 with the Van Leer flux-splitting method on different resolutions.

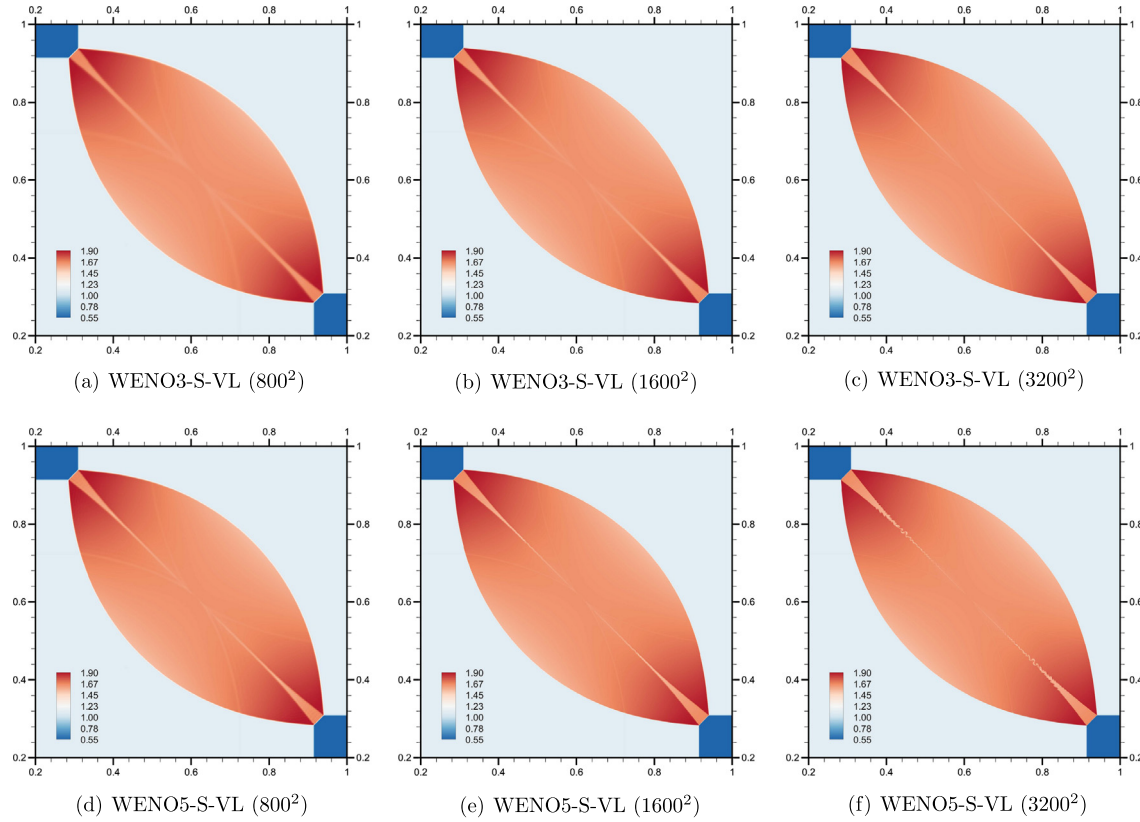


Fig. 18. Configuration 4 of Lax and Liu [19] at time $t = 0.25$. Density fields obtained by using the WENO3 and WENO5 with the Van Leer flux-splitting method on different resolutions.

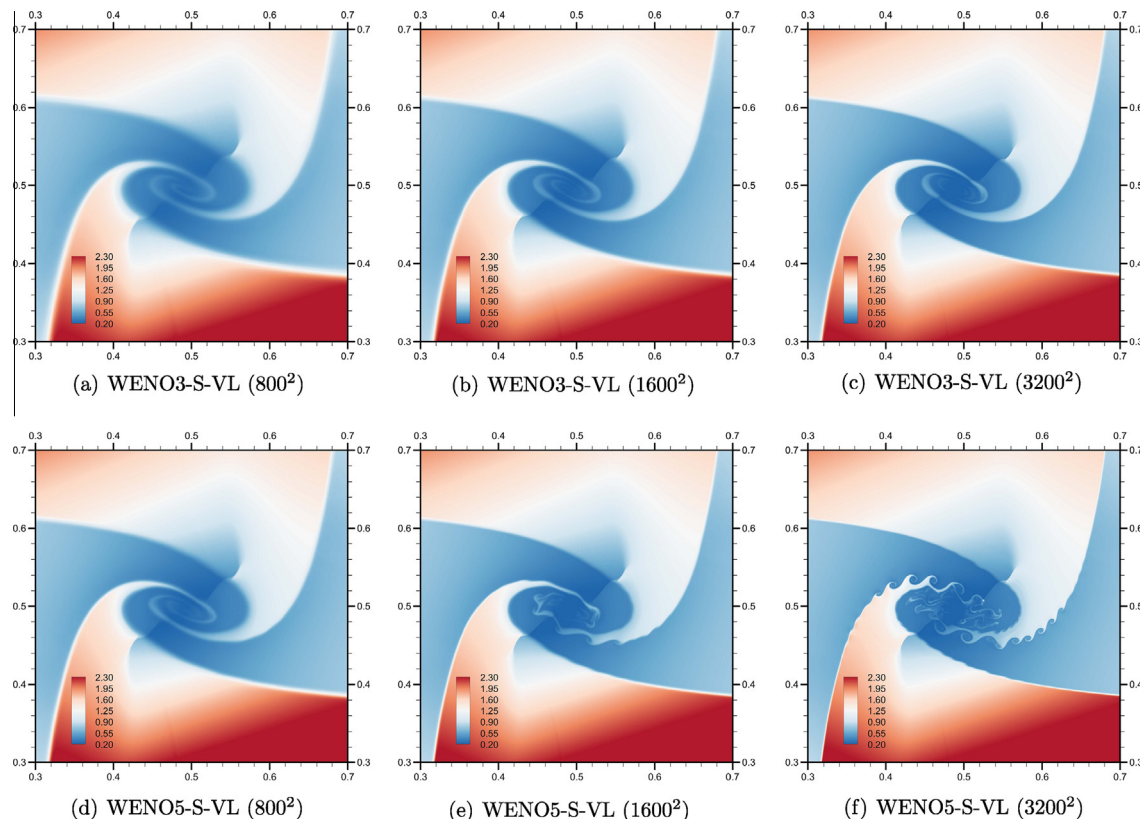


Fig. 19. Configuration 6 of Lax and Liu [19] at time $t = 0.25$. Density fields obtained by using the WENO3 and WENO5 with the Van Leer flux-splitting method on different resolutions.

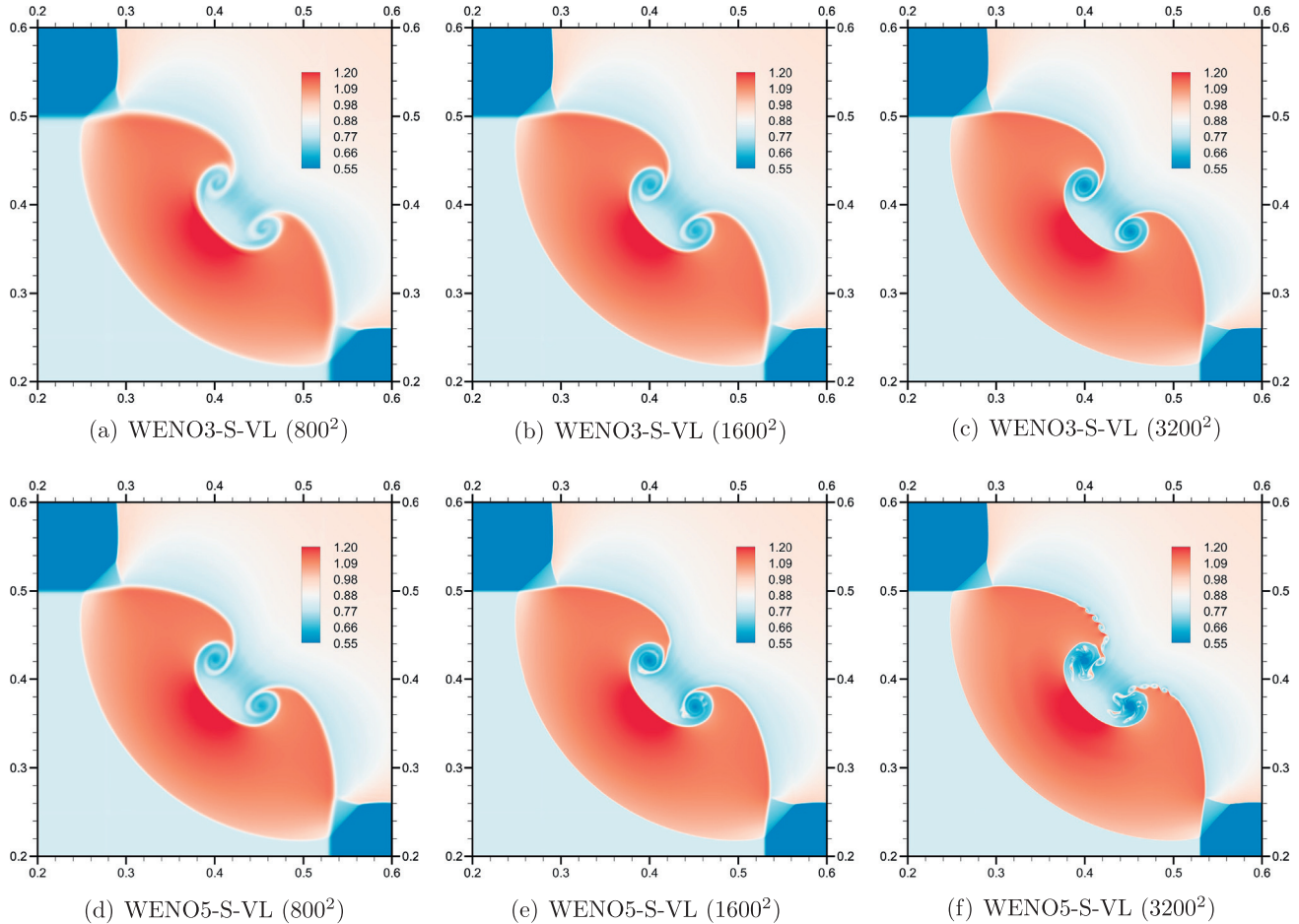


Fig. 20. Configuration 11 of Lax and Liu [19] at time $t = 0.3$. Density fields obtained by using the WENO3 and WENO5 with the Van Leer flux-splitting method on different resolutions.

interface normal velocity in directions tangential to the shock where this component of velocity is low.

In addition to these contour plots, we also present error norms in order to quantify the results. Using the difference between high-resolution reference solution and computed solutions, we compute the mean discrete L^2 norms of the density field as

$$\|L^2(\rho)\| = \frac{1}{N_x N_y} \sum_{i=1}^{N_x} \sum_{j=1}^{N_y} |\rho_{i,j}^{\text{ref}} - \rho_{i,j}|^2 \quad (54)$$

where ρ^{ref} is the reference solution obtained by the MUSCL-KT scheme on a resolution of 3200^2 . It should be noted that we evaluate the reference solution data at the discrete points corresponding to the coarse grid with $N_x = N_y = 400$. The computed discrete L^2 norms of the density field are tabulated in Table 1 for both configurations yielding consistent results with the demonstrations presented in Figs. 7 and 8.

Second, we focus on performance of reconstruction schemes in more detail using the same flux-limiter and Riemann solver. In all the cases presented in Figs. 9 and 10, the Van Albada flux-limiter and the Rusanov's approximate Riemann solver are jointly utilized in the various forms of MUSCL reconstructions. The third-order WENO reconstruction scheme is also included for comparison purposes. We also included the results obtained by the first-order reconstruction scheme given by Eq. (7). First of all, the first-order scheme shows excessive dissipation compared to the all forms of higher-order MUSCL schemes. Figs. 9 and 10 clearly demonstrate that the type of reconstruction is not as dominant as the other

factors (i.e., type of the flux-limiter or type of the Riemann solver) when designing a shock capturing compressible flow solver. This behavior can also be seen from Table 2 showing errors in density.

Next, we examine the effects of flux-limiters on the MUSCL reconstruction schemes. In order to minimize the numerical dissipation due to the Riemann solver, we explored several limiters to preserve the monotonicity of our solutions by using the Roe's approximate Riemann solver in our joint solvers. Solving the case with Configuration 3 and Configuration 12, Figs. 11 and 12 demonstrates results for the MUSCL scheme using a unique third-order accurate reconstruction with $\kappa = 1/3$. Similar analysis with MUSCL-KT scheme is also shown in Figs. 13 and 14 for Configuration 3 and Configuration 12 test problems, respectively. We show that results are also highly dependent to the choice of the flux-limiters which work by interpolating between the flux calculated by a reduced-order scheme and the flux calculated by a higher-order scheme. Tables 3 and 4 also show that a proper selection of the flux-limiter function affects solutions more than the type of the interpolation procedure in MUSCL reconstructions. The underpinning idea in flux limiting is that oscillations near a discontinuity can be eliminated by making the approximation mimic a first order-scheme near a steep gradient using a flux-limiter, while higher order accuracy is achieved in smoother regions. Although MUSCL schemes with superbee limiter yield smaller L^2 norm, it is clear from the figures that the non-dissipative superbee flux-limiter along with the Roe solver does not provide enough dissipation to damp spurious signals. Although the superbee limiter produces the sharpest possible gradients while still being TVD, we suggest

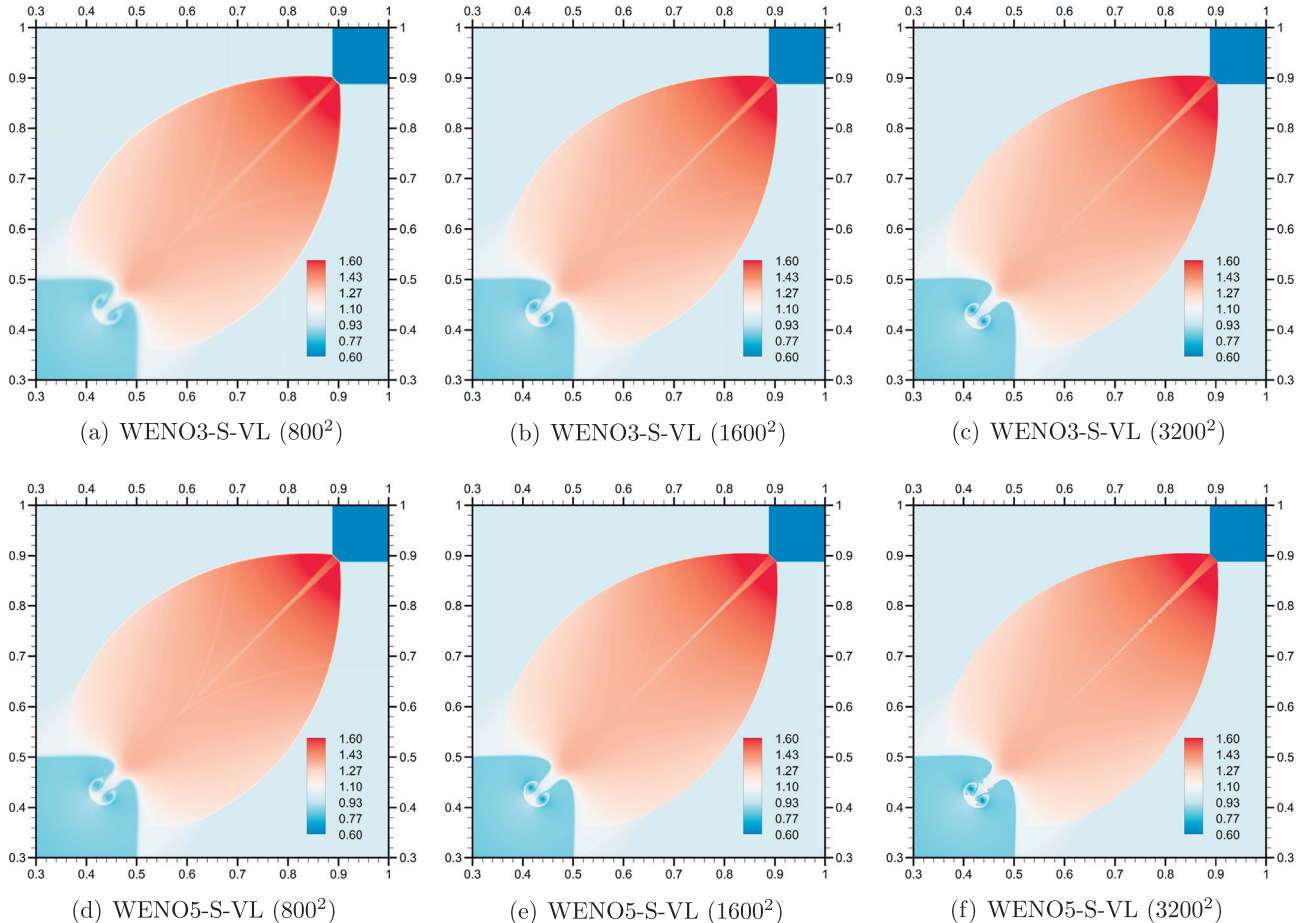


Fig. 21. Configuration 12 of Lax and Liu [19] at time $t = 0.25$. Density fields obtained by using the WENO3 and WENO5 with the Van Leer flux-splitting method on different resolutions.

to use a flux-limiter showing some form of the dissipative behavior (e.g., Van Leer or Van Albada limiters) to eliminate amplified cross-coupling perturbations.

Finally, we investigate the performance of flux-splitting procedures in five-point stencil WENO schemes. In Figs. 15 and 16 we compare various forms of flux-splitting WENO schemes which they do not require to use a Riemann solver at the cell interfaces. For comparison purposes, we also include results for the reconstruction based WENO scheme with Roe's Riemann solver, WENO3-R-Roe. For the flux-splitting WENO solvers based on the smoothness indicators, we observe that the results show negligible sensitivity to the flux-splitting procedure. However, Table 5 demonstrates that the Van Leer flux-splitting yields slightly more accurate results. We also demonstrate that the reconstruction based WENO scheme with Roe solver is more accurate than all the versions of the flux-splitting WENO solvers tested in this study.

4.2. The performance of the third- and fifth-order flux-splitting WENO schemes

In this section, we investigate the effects of the order of accuracy on the solution for using the third-order (total five-point stencil) and fifth-order (total seven-point stencil) WENO schemes for solving two-dimensional Riemann problems. Similar to our previous analysis, the performances of these high-resolution solvers are compared for several carefully selected test cases described by Lax and Liu [19]. Although we investigated four flux-splitting schemes described in Section 3.2, it is found that the use of the

WENO scheme with the van Leer flux vector splitting scheme provides solutions for a variety of benchmark problems with slightly better accuracy. Therefore, we only present results obtained by the third-order WENO3-S-VL and the fifth-order WENO5-S-VL solvers.

In order to show the effects of the various resolution on both the third-order and fifth-order WENO schemes for different flow configurations described in Fig. 2, we demonstrate the six sets of comparisons in a consistent way. Fig. 17 shows the density contours for the structure of four shocks producing a narrow jet; Fig. 18 demonstrates another problem involving four shocks; the problem shown in Fig. 19 involves four contact discontinuities; the problems shown in Figs. 20 and 21 involve two shocks and two contact discontinuities; and the final problem shown in Fig. 22 involves two contact discontinuities, a rarefaction as well as a shock wave. We use the same comparison methodology in all these configurations for which the results obtained by the third-order WENO schemes are shown in top panels, and bottom panels represent those obtained by the fifth-order WENO schemes. The resolutions increase from left to right. In all figures, we plot the continuous density levels using the same layouts for each problem in order to highlight the differences among the joint solvers.

Performing benchmark quality high-resolution computations, we demonstrate that the solutions are quite dependant to the order of accuracy. The fifth-order WENO scheme produce solutions with small-scale vortical flow structures for higher resolutions which are usually associated with the high Reynolds number

viscous flows. For example, as shown in Fig. 17, small vortices are developed along the slip line which agree well with the results documented by Baeza et al. [55] using an adaptive mesh refinement method with 2048^2 resolution. According to our computations, it is important that these Kelvin–Helmholtz instability like vortical structures are not captured in any forms of the third-order WENO schemes at any resolution being considered.

We surprisingly find that there is no development of these small scale vortical structures when using the third-order WENO schemes equipped with all form of splitting procedure tested in this study, even with a quite high resolution of 3200^2 for all the flow configurations tested here. For example, results of Figs. 17 and 19, WENO5-S-VL clearly shows the Kelvin–Helmholtz instabilities at 1600^2 resolution while using WENO3-S-VL there is no sign of instability at much higher 3200^2 resolution. Based on our numerical experiments performed here, we emphasize that it is not possible to make a general conclusion whether it is possible to capture these small-scale vortical structures using high enough spatial resolution or not by using the five-point stencil methods such as MUSCL or WENO3 schemes. However, our results clearly demonstrate the resolving power of the higher order WENO schemes which can be determined by the number of small vortical structures that can be captured along the discontinuous slip lines. Although the Euler equations represent the inviscid flows, the upwinding in shock capturing algorithms add the numerical dissipation to the system. The difference between the third- and fifth-order schemes would be explained in following way. First, it is well known from the spectral analysis that the amount of numerical

Table 6

The total CPU costs (in h) for several shock capturing schemes considered in this study.

Resolution	MUSCL-KT	WENO3-R	WENO3-S-VL	WENO5-S-VL
400^2	0.1961	0.2335	0.1614	0.2490
800^2	1.6411	1.9611	1.3747	2.1302
1600^2	14.3873	17.1066	12.4862	18.9391
3200^2	137.1953	156.0613	111.9615	175.8576

dissipation added to the Euler system by the fifth-order order scheme are smaller than that of the third-order scheme. Second, increasing the resolution results in reducing the effective dissipation range. Consequently, the artificial cell Reynolds number in high-order schemes becomes higher and higher by increasing the order of accuracy and resolution. Therefore, the solution convect the vorticity and generate small-scale vortical flow structures similar to those observed in high Reynolds number turbulent flows. Since the vorticity is generated as a result of a discontinuity in the flow field, these solutions can be considered valid and accurate solutions to the Euler equations.

In all the cases considered here, we showed that the vorticity may be created as a result of a discontinuity in the flow or it may result from numerical dissipation error in the computational technique which is another mechanism for creating vorticity. Usually we attempt to eliminate all of the computational errors, although it may not always be possible since all numerical

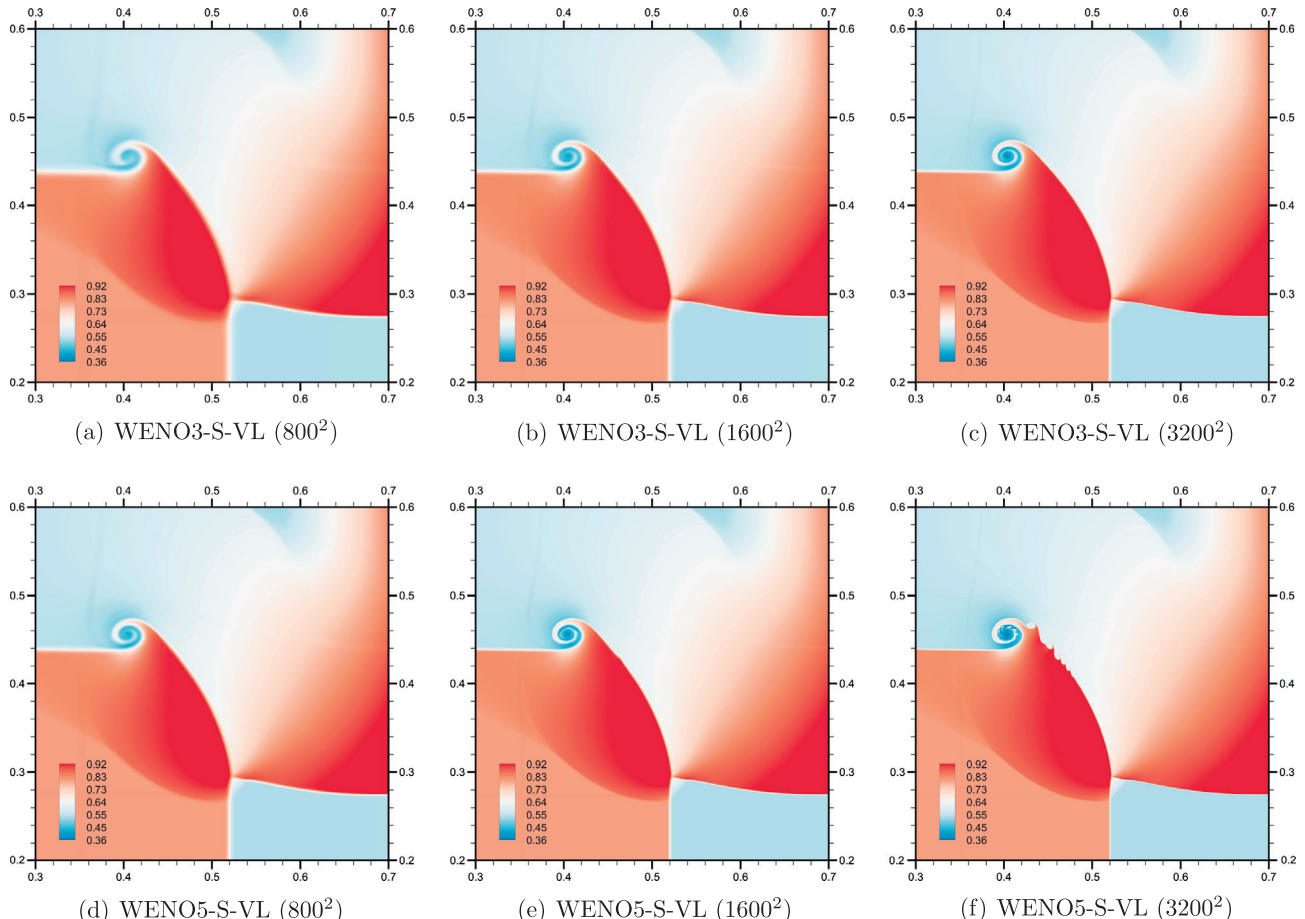


Fig. 22. Configuration 15 of Lax and Liu [19] at time $t = 0.2$. Density fields obtained by using the WENO3 and WENO5 with the Van Leer flux-splitting method on different resolutions.

schemes for the Euler equations require some level of artificial dissipation due to upwinding towards the wave propagation direction. When vorticity is generated as a result of a discontinuity in the flow, as we see from the high-resolution high-order accurate numerical simulations of the Euler equations, the use of at least a fifth-order accurate scheme is required to capture underlying physics with wave disturbances. Therefore, we conclude that the development of high-order algorithms is critical to convect these small-scale vortical structures without damping in time. Our results could also be considered a starting motivation for designing implicit large-eddy simulation (ILES) algorithms for high Reynolds number compressible flows, a topic we intend to investigate further in a future study. ILES is a so-called no turbulence model assuming that the numerics provide sufficient modeling of the subgrid terms to allow the correct amount dissipation of turbulent kinetic energy (see [17] for a comprehensive review). Numerical methods for solving the Euler equations usually add numerical dissipation to discrete system in order to ensure stability by producing a vanishing viscosity flow solution. This artificial dissipation disappears in the limit of mesh size tending to zero remaining consistent with the governing equations. We also address [56,57] for extensive discussions and derivations of physical basis for the form of artificial dissipations in the cell-centered shock capturing finite volume methods in which the numerical grid is assumed to be equivalent to a top hat filter in physical space.

Finally, we present the computational efficiencies of the various shock capturing schemes considered in this study. All computations were carried out using the gfortran compiler on a Linux cluster system made up of quad-core Intel Xeon X5355 (2.66 GHz/node). The total CPU costs (in hours) for the third-order and the fifth-order Van Leer flux-splitting WENO schemes which are listed in Table 6 for various resolutions. The CPU times for the reconstruction based schemes that use the Rusanov's Riemann solver are also included. Although we have not attempted any special efforts for writing optimal code, we can conclude that the splitting based approaches are slightly more efficient than the reconstruction based approaches. Table 6 also shows that the computational cost of the fifth-order WENO scheme is around 1.5 times higher than the cost of the third-order WENO scheme. We also note here that the CPU cost approximately increases by a factor of eight with double the resolution in each direction, which can be considered as an optimal scaling ratio for the fixed CFL number computations over a two-dimensional domain.

5. Conclusions

This study investigates the performance of high-resolution schemes for hyperbolic conservation laws by solving two-dimensional Riemann problems for the Euler equations in gas dynamics. Several variants of flux-limiter based MUSCL reconstruction procedures are compared to the WENO reconstruction procedure which is based on the idea of nonlinear weights with the smoothness indicators. The effects of several reconstruction procedures are investigated in combination with various Riemann solvers at the cell interfaces. The performances of local Lax–Friedrichs, Steger and Warming and Van Leer flux-splitting procedures on the accuracy of the third- and fifth-order WENO schemes are also tested and compared on different resolutions. The joint solvers are applied to several Riemann problems including shock and rarefaction waves as well as contact discontinuities. It is shown that Roe solvers are less dissipative than the Rusanov solver for the reconstruction based schemes in which results are also highly dependent to the choice of the flux-limiter. We show that the non-dissipative superbee flux-limiter along with the Roe solver does not provide

enough dissipation to damp spurious signals. Thus, we suggest to use a flux-limiter showing some form of the dissipative behavior. In assessments of the flux-splitting WENO solvers, we observe that the results show negligible sensitivity to the flux-splitting procedure. We also demonstrate that the reconstruction based WENO scheme with Roe solver is more accurate than all the versions of the flux-splitting WENO solvers tested in this study. Performing benchmark quality high-resolution computations, it is shown that the Euler equations discretized by the fifth-order WENO scheme with all the forms of splitting methods produce solutions which convect vorticity and create small-scale vortical flow structures which are usually associated with the high Reynolds number viscous flows. These Kelvin–Helmholtz instability like vortical structures are not captured in any forms of the third-order WENO schemes for the considered resolutions. Since the vorticity is generated as a result of a discontinuity in the flow field, these solutions can be considered valid and accurate solutions to the Euler equations.

References

- [1] Harten A. High resolution schemes for hyperbolic conservation laws. *J Comput Phys* 1983;49(3):357–93.
- [2] Sweby PK. High resolution schemes using flux limiters for hyperbolic conservation laws. *SIAM J Numer Anal* 1984;21(5):995–1011.
- [3] Anderson WK, Thomas JL, Van Leer B. Comparison of finite volume flux vector splittings for the Euler equations. *AIAA J* 1986;24(9):1453–60.
- [4] Harten A, Osher S, Engquist B, Chakravarthy SR. Some results on uniformly high-order accurate essentially nonoscillatory schemes. *Appl Numer Math* 1986;2(3):347–77.
- [5] Yee HC. Construction of explicit and implicit symmetric TVD schemes and their applications. *J Comput Phys* 1987;68(1):151–79.
- [6] Harten A, Engquist B, Osher S, Chakravarthy SR. Uniformly high order accurate essentially non-oscillatory schemes, III. *J Comput Phys* 1987;71(2):231–303.
- [7] Yamamoto S, Daiguji H. Higher-order-accurate upwind schemes for solving the compressible Euler and Navier–Stokes equations. *Comput Fluids* 1993;22(2):259–70.
- [8] Shu CW. High order weighted essentially nonoscillatory schemes for convection dominated problems. *SIAM Rev* 2009;51(1):82–126.
- [9] Pirozzoli S. Numerical methods for high-speed flows. *Ann Rev Fluid Mech* 2011;43:163–94.
- [10] Roe PL. Approximate Riemann solvers, parameter vectors, and difference schemes. *J Comput Phys* 1981;43(2):357–72.
- [11] Harten A, Lax PD, Van Leer B. On upstream differencing and Godunov-type schemes for hyperbolic conservation laws. *SIAM Rev* 1983;25(1):35–61.
- [12] Jiang GS, Shu CW. Efficient implementation of weighted ENO schemes. *J Comput Phys* 1996;126:202–28.
- [13] Garnier E, Mossi M, Sagaut P, Comte P, Deville M. On the use of shock-capturing schemes for large-eddy simulation. *J Comput Phys* 1999;153(2):273–311.
- [14] Liska R, Wendroff B. Comparison of several difference schemes on 1D and 2D test problems for the Euler equations. *SIAM J Scient Comput* 2003;25(3):995–1017.
- [15] Greenough JA, Rider WJ. A quantitative comparison of numerical methods for the compressible Euler equations: fifth-order WENO and piecewise-linear Godunov. *J Comput Phys* 2004;196(1):259–81.
- [16] Kurganov A, Lin CT. On the reduction of numerical dissipation in central-upwind schemes. *Commun Comput Phys* 2007;2(1):141–63.
- [17] Thornber B, Mosedale A, Drikakis D. On the implicit large eddy simulations of homogeneous decaying turbulence. *J Comput Phys* 2007;226(2):1902–29.
- [18] Johnsen E, Larsson J, Bhagatwala AV, Cabot WH, Moin P, Olson BJ, et al. Assessment of high-resolution methods for numerical simulations of compressible turbulence with shock waves. *J Comput Phys* 2010;229(4):1213–37.
- [19] Lax PD, Liu XD. Solution of two-dimensional Riemann problems of gas dynamics by positive schemes. *SIAM J Scient Comput* 1998;19(2):319–40.
- [20] Lax PD. Weak solutions of nonlinear hyperbolic equations and their numerical computation. *Commun Pure Appl Math* 1954;7(1):159–93.
- [21] Steger JL, Warming RF. Flux vector splitting of the inviscid gas dynamic equations with application to finite-difference methods. *J Comput Phys* 1981;40(2):263–93.
- [22] Van Leer B. Flux-vector splitting for the Euler equations. In: Krause E, editor. Eighth international conference on numerical methods in fluid dynamics. Springer; 1982. p. 507–12.
- [23] Thompson PA. Compressible fluid dynamics. McGraw-Hill; 1972.
- [24] Van Der Burg JW, Kuerten JGM, Zandbergen PJ. Improved shock-capturing of Jameson's scheme for the Euler equations. *Int J Numer Meth Fluids* 1992;15(6):649–71.
- [25] Parent B. Positivity-preserving high-resolution schemes for systems of conservation laws. *J Comput Phys* 2012;231(1):173–89.

- [26] Shu CW, Osher S. Efficient implementation of essentially non-oscillatory shock-capturing schemes. *J Comput Phys* 1988;77(2):439–71.
- [27] Gottlieb S, Shu CW. Total variation diminishing Runge–Kutta schemes. *Math Comput* 1998;67(221):73–85.
- [28] Gottlieb S, Shu CW, Tadmor E. Strong stability-preserving high-order time discretization methods. *SIAM Rev* 2001;43(1):89–112.
- [29] Borges R, Carmona M, Costa B, Don WS. An improved weighted essentially non-oscillatory scheme for hyperbolic conservation laws. *J Comput Phys* 2008;227(6):3191–211.
- [30] Hu XY, Wang Q, Adams NA. An adaptive central-upwind weighted essentially non-oscillatory scheme. *J Comput Phys* 2010;229(23):8952–65.
- [31] Kara K, Balakumar P, Kandil OA. Effects of nose bluntness on hypersonic boundary-layer receptivity and stability over cones. *AIAA J* 2011;49(12):2593–606.
- [32] Feng H, Hu F, Wang R. A new mapped weighted essentially non-oscillatory scheme. *J Scient Comput* 2012;51(2):449–73.
- [33] San O, Staples AE. High-order methods for decaying two-dimensional homogeneous isotropic turbulence. *Comput Fluids* 2012;63:105–27.
- [34] Van Leer B. Towards the ultimate conservative difference scheme. II. Monotonicity and conservation combined in a second-order scheme. *J Comput Phys* 1974;14(4):361–70.
- [35] Van Leer B. Towards the ultimate conservative difference scheme. III. Upstream-centered finite-difference schemes for ideal compressible flow. *J Comput Phys* 1977;23(3):263–75.
- [36] Van Leer B. Towards the ultimate conservative difference scheme. V. A second-order sequel to Godunov's method. *J Comput Phys* 1979;32(1):101–36.
- [37] Tannehill JC, Anderson DDA, Pletcher RH. Computational fluid mechanics and heat transfer. Taylor & Francis; 1997.
- [38] Knight DD. Elements of numerical methods for compressible flows. Cambridge University Press; 2006.
- [39] Hirsch C. Numerical computation of internal and external flows: the fundamentals of computational fluid dynamics. Butterworth-Heinemann; 2007.
- [40] Van Albada GD, Van Leer B, Roberts WW. A comparative study of computational methods in cosmic gas dynamics. *Astron Astrophys* 1982;108:76–84.
- [41] Roe PL. Characteristic-based schemes for the Euler equations. *Ann Rev Fluid Mech* 1986;18(1):337–65.
- [42] Fromm JE. A method for reducing dispersion in convective difference schemes. *J Comput Phys* 1968;3(2):176–89.
- [43] Nessyahu H, Tadmor E. Non-oscillatory central differencing for hyperbolic conservation laws. *J Comput Phys* 1990;87(2):408–63.
- [44] Kurganov A, Tadmor E. New high-resolution central schemes for nonlinear conservation laws and convection-diffusion equations. *J Comput Phys* 2000;160(1):241–82.
- [45] Titarev VA, Toro EF. WENO schemes based on upwind and centred TVD fluxes. *Comput Fluids* 2005;34(6):705–20.
- [46] Ruasnov VV. Calculation of intersection of non-steady shock waves with obstacles. *USSR Comput Math Math Phys* 1961;1:267–79.
- [47] Toro EF. Riemann solvers and numerical methods for fluid dynamics: a practical introduction. Springer; 2009.
- [48] LeVeque RJ. Finite volume methods for hyperbolic problems. Cambridge University Press; 2002.
- [49] Godunov SK. A difference method for numerical calculation of discontinuous solutions of the equations of hydrodynamics. *Matematicheskii Sbornik* 1959;89(3):271–306.
- [50] Liu XD, Osher S, Chan T. Weighted essentially non-oscillatory schemes. *J Comput Phys* 1994;115(1):200–12.
- [51] Xing Y, Shu CW. High order finite difference WENO schemes with the exact conservation property for the shallow water equations. *J Comput Phys* 2005;208(1):206–27.
- [52] Crnarić-Žic N, Vučović S, Sopta L. On different flux splittings and flux functions in WENO schemes for balance laws. *Comput Fluids* 2006;35(10):1074–92.
- [53] Deng X, Mao M, Tu G, Zhang Y, Zhang H. Extending weighted compact nonlinear schemes to complex grids with characteristic-based interface conditions. *AIAA J* 2010;48(12):2840–51.
- [54] Laney CB. Computational gas dynamics. Cambridge University Press; 1998.
- [55] Baeza A, Martínez-Gavara A, Mulet P. Adaptation based on interpolation errors for high order mesh refinement methods applied to conservation laws. *Appl Numer Math* 2012;62(4):278–96.
- [56] Margolin LG, Rider WJ, Grinstein FF. Modeling turbulent flow with implicit LES. *J Turbul* 2006(7):1–27.
- [57] Grinstein FF, Margolin LG, Rider WJ. Implicit large eddy simulation: computing turbulent fluid dynamics. Cambridge University Press; 2007.